Lehrstuhl für Technische Mechanik
Friedrich-Alexander-Universität
Erlangen-Nürnberg

MASTER THESIS

# A Study on the Emergence of Ferroelectricity

Dan Wang

Erlangen, December 15, 2017

Examiner:     Prof. Dr.-Ing. habil. Paul Steinmann
Advisor:       Vishal Boddu

# Eidesstattliche Erklärung / Statutory Declaration

Hiermit versichere ich eidesstattlich, dass die vorliegende Arbeit von mir selbständig, ohne Hilfe Dritter und ausschließlich unter Verwendung der angegebenen Quellen angefertigt wurde. Alle Stellen, die wörtlich oder sinngemäß aus den Quellen entnommen sind, habe ich als solche kenntlich gemacht. Die Arbeit wurde bisher in gleicher oder ähnlicher Form keiner anderen Prüfungsbehörde vorgelegt.

I hereby declare formally that I have developed and written the enclosed thesis entirely by myself and have not used sources or means without declaration in the text. Any thoughts or quotations which were inferred from the sources are marked as such. This thesis was not submitted in the same or a substantially similar version to any other authority to achieve an academic grading.

Erlangen, December 15, 2017

[Dan WANG]

iv

# Abstract

Ferroelectricity is a characteristic of certain materials showing a spontaneous polarization that can be reversed by the application of a changing external electric field. The spontaneous polarization of ferroelectric materials implies a hysteresis effect which can be used as a memory function, and ferroelectric capacitors are currently being used to make Ferroelectric Random Access Memory (FRAM). In these applications thin films of ferroelectric materials are typically used, as this allows the field required to switch the polarization to be achieved with a moderate voltage. Additionally, miniaturization of such films allows for storing a large amount of memory. However, it is known that ferroelectricity weakens as the thickness of ferroelectric slab reduces.

The aim of this work is to study the emergence of ferroelectricity in thin films by performing atomistic simulations. Barium titanate single crystal thin film is chosen for this study due to its simple perovskite structure. Ferroelectricity is observed by plotting electric polarization under the influence of external electric field. These plots are obtained for various thicknesses of thin films to identify the thickness of thin film such that there is a noticeable ferroelectric hysteresis. This thesis concludes that the ferroelectricity emerges in thin films as thin as 48 Å.

# CONTENTS

# 1

# INTRODUCTION

The investigators and researchers gave the materials, on which this work concerns, the name as "ferroelectrics" because of its specific material behaviors, of which polarization in microscopic view is comparable to the one for dielectric media in macroscopic view and the hysteresis loop is analogous to the magnetic hysteresis (such as iron with a changing magnetic field). Due to its properties, ferroelectrics can be utilized to store information as "0" or "1" with the changing of external electric field. It is the reason why it takes only decades for ferroelectrics to pervade many aspects of our daily live.

## 1.1 History

With the discoveries of the different ferroelectrics, the fundamental ferroelectric properties were studied gradually: the spontaneous polarization and the reorientation of the spontaneous polarizations with the changing electric fields. These properties are explained in section 2.2.1 and 2.2.2. This section briefly introduces the history of the investigations of the ferroelectrics.

## 1.1.1 Single-crystal Material

In 1660s, the first kind of ferroelectric material, known as Rochelle salt (sodium postassium tartrate tetrahydrate, $NaKC_4H_4O_6 \cdot 4H_2O$), was developed for medicinal purposes by Elie Seignette in La Rochelle, France [Wadhawan, 2000]. After Sir David Brewster gave the effect, the polarization disappears for the stable temperature [Lalena and Cleary, 2010], the name – pyroelectricity (thermal–polar properties) in 1824, and William Thomson perfected the theory, temperature changes produce elastic strains within or between doublets with assuming the pyroelectric material as a large number of "electrical doublets", in 1878 [Lang, 1974], the Curies began to investigate the piezoelectricity (stress–polar properties) of $NaKC_4H_4O_6 \cdot 4H_2O$ and other minerals in the 1880s [Buchanan, 2004]. 40 years later, Josphe Valasek discovered the ferroelectricity, the main topic this work concerns of, in Rochelle salt [Fousek, 1991].

However, Rochelle salt was the only known ferroelectric in existence for well over a decade. The ferroelectric property, as a rare phenomenon, only was attributed to the dipolar interaction between the water molecules in $NaKC_4H_4O_6 \cdot 4H_2O$. The material was popular since it was readily available and easily grown as large single crystals of excellent optical quality but useless for its water solubility [Haertling, 1999].

The production of phosphates and arsenate of potassium, of which the best known one is $KH_2PO_4$, in 1935 by Busch and Scherrer and 1938 by Busch changed the perception. The intermolecular $O - H \cdots O$ hydro bonding of the simpler crystal structure without any water exhibits the different orientations of the $(H_2PO_4)^-$ dipoles. It led Slater to give the basis of the first microscopic theory of ferroelectricity in 1941.

The notion of requirement of hydrogen bonding for the ferroelectricity was discarded after $BaTiO_3$, a even much simpler crystal structure without hydrogen bonding found by Megaw in 1945. At first, $BaTiO_3$ was established as a new type of ceramic capacitor with K > 1100 for some military purposes in World War II. The observation by von Hippel's group at the Massachusetts Institute of Technology in [Von Hippel et al., 1946], a milestone in the history of ferroelectric research, indicated the perovskite material $BaTiO_3$ is ferroelectric.

Some other, now well-known, members in the perovskite structural family were also verified to be ferroelectric, such as $KNbO_3$ found by Matthias in 1949, $LiNbO_3$ found by Matthias and Remeika in 1949 and $PbTiO_3$ found by Shirane et al. in 1950.

In 1937, Landau had put forward the phenomenological theory of phase transitions on the theoretical front. He was the first to apply group-theoretical ideas to thermodynamics. A more detailed introduction of Landau's theory can be found in section 2.2.3.

For more imformation, the reader is pointed to [Wadhawan, 2000] and [Haertling, 1999].

## 1.1.2 Thin Film

There is a dawning realization that the smaller sizes of the ferroelectric materials display ferroelectricity implied that the more information can be stored [Lichtensteiger et al., 2007]. That is why the late 1960s and early 1970s witnessed the development of ferroelectric thin films for its extensive use in memory device [Okuyama and Ishibashi, 2005, Setter et al., 2006] .

Feuersanger is the pioneer to find that in the $BaTiO_3$ films prepared by electron-beam evaporation, the tetragonal phase could only be observed at room temperature for the thickness of the films in the order of magnitude of -7 m, which implied the phase is unstable when the thickness of the thin films less than 0.1 $\mu$m in [Feuersanger et al., 1964]. Slack and Burfoot decreased the thickness to 200Å with $BaTiO_3$ grown by flash evaporation and found the switchable polarisation values were about $20\%$ of the bulk crystal one in [Slack and Burfoot, 1970]. Batra and Silverman at IBM published the ferroelectric polar state was thermodynamically unstable below a certain critical thickness which was calculated to be 0.4 $\mu$m for triglycine sulphate and the case would be even worse for metallic electrodes in [Batra and Silverman, 1972]. The measurements on vacuum-deposited $BaTiO_3$ films showed sharp, well-defined dielectric anomalies near 120° down to film thickness of 0.023 $\mu$m by Tomashpolski in 1974, as [Rabe et al., 2007] mentioned. For a film thickness of 0.01 $\mu$m this anomaly disappeared but the anomaly at the transition near 0 °C. But Line and Glass mentioned the problem of the thinnest thickness in experiment in that time might be the problem of defects in films prepared by different techniques and the disappearance of the dielectric anomaly at 120 $°C$ for film thickness below about 0.023 $\mu$m may thus be evidence of the ferroelectric phase becoming unstable owing to the finite size effect [Lines and Glass, 1977] . In 1984, Tilley and Zeks analyzed the changing polarizations with the boundary conditions at the surfaces of a film of thickness L are given by means of an extrapolation length $\delta$ and the nature of the phase transition [Tilley and Žekš, 1984]. Chen indicated the constants in Tilley and Zek's paper could be gotten in 1999 [Chen et al., 1999]. The limit of the thickness of polymer films was down to 10 Å in [Bune et al., 1998]. The measurements of Tybell et al. revealed the ferroelectric state of $Pb(Zr_{0.2}Ti_{0.8})O_3$ for 40Å-thick films is stable [Tybell et al., 1999]. Later, Ghosez and Rabe found (001) $PbTiO_3$ films as thin as three unit cells exhibited a perpendicularly polarized ferroelectric ground state, with significant enhancement of the polarization at the surface [Ghosez and Rabe, 2000]. First-principles calculation showed that $BaTiO_3$ films with $SrRuO_3$ electrodes lose ferroelectricity below 24 Å (6 unit cells) in [Junquera and Ghosez, 2003]. Fong et al. reported the ferroelectric phase is stable for thicknesses of $PbTiO_3$ down to 3 unit cells (12 Å) at room temperature, but the result with 6-unit-cell-film at $T_c$ will be better [Fong et al., 2004]. Sai et al. presented ab-initio demonstration of realistic electrodes stabilizing polarization normal to the surface in ultra-thin films of less than 10 Å thick and the behaviour in $BaTiO_3$ is not universal to all ferroelectric thin films [Sai et al., 2005]. Sang et al. mentioned the spontaneous polarizations in z-direction of different thicknesses (2.8 nm, 3.6 nm, 4.4 nm) ferroelectric film with NPT (isothermal and isotonic system) ensembles shows both different thicknesses and in-plane strains will influence the polarization distribution pattern [Sang et al., 2008].

The decreasing orders of magnitude of the experimentally obtained minimum thickness for the ferroelectric thin film showed the problem is mainly about the limitations of the quality, as the assumptions of Line and Glass.

In theory, the Landau model for $BaTiO_3$ films epitaxially grown onto cubic substrates [Scott and De Araujo, 1989], giving distinct phases (so-called c-, a- and ac-phases) due to misfit strain was developed by Pertsev in 2000 [Scott, 2013].

### 1.1.3 Molecular Simulation

The field of molecular simulation began in precursory form with Heisenberg's paper of quantum mechanics in 1925. After Schrrodinger wave equation was published in 1926 and molecular orbital put forward by Mulliken and Hund in 1932, quantum chemistry, as a new discipline, has been created. The model of water molecule was found by Bernal and Flowler in [Bernal and Fowler, 1933] and Hill said the molecular energy could be calculated by the van der Waals attraction and the deformations of bond lengths and bond angles in 1946 [Maranas and Floudas, 1994].

With the foundation of molecular simulation, molecular dynamics started with a whimper. Alder and Wainwright carried out the first condensed-phase molecular dynamics calculation on a hard-sphere system in 1957, showing that a solid–liquid phase transition exists [Tuckerman, 2010]. The first simulations of a realistic continuous potential for systems of 864 argon atoms were finished by Rahman in 1964 and Verlet in 1967. Molecular dynamics simulations of diatomic liquids characterized by the time dependence of molecular reorientation were done by Harp and Berne. The first molecular dynamics simulations of liquid water were completed by Stillinger and Rahman in 1971. The first molecular dynamics calculations of proteins were published by Karplus and his co-workers. Explicit treatment of molecular systems was enabled by the introduction of techniques for maintaining specific bonding patterns either by stiff intramolecular forces in 1970 or by imposing holonomic constraints into the simulation by Ryckaert and his coworkers in 1977 [Tuckerman, 2010]. The technique of ab-initio or first-principles molecular dynamics signaled the new era of molecular simulation by Car and Parrinello in 1985.

For more imformation, the reader is pointed to [Tuckerman, 2010].

## 1.2 Application

### 1.2.1 Ferroelectric Ceramic

The ferroelectric material became scientifically and industrially important as Gray found the domain within the grains of the material would be oriented by the external electric field in 1945 [Haertling, 1999]. After three significant discoveries of unusually high dielectric constant of $BaTiO_3$, the origin of the high dielectric constant depending on ferroelectric
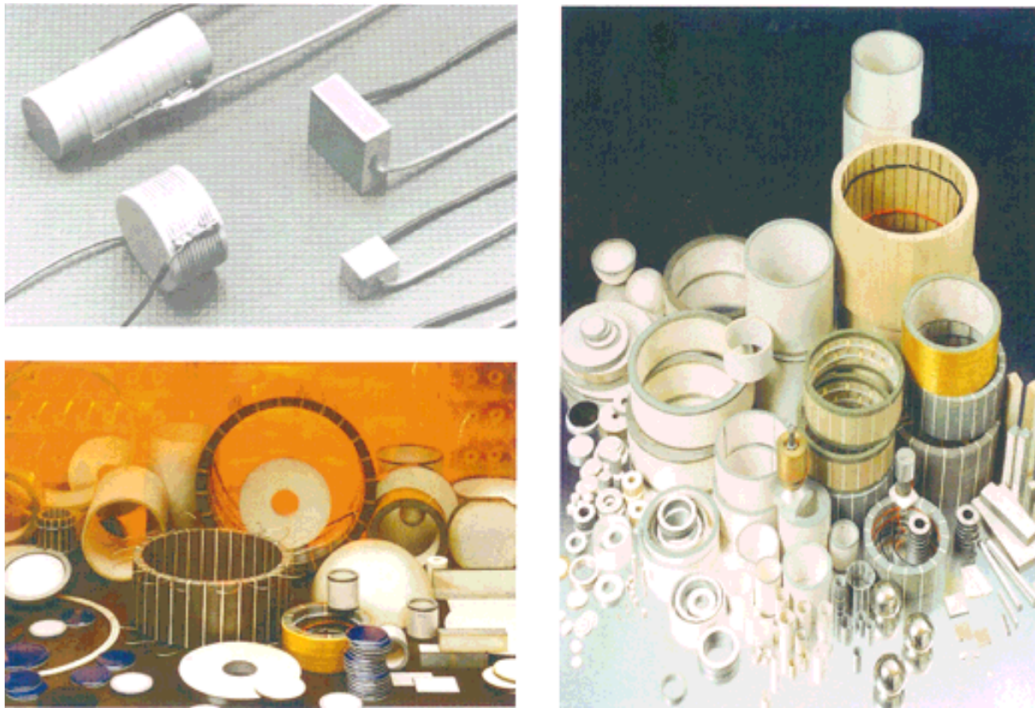
**Figure 1.1:** Variety of Ferroelectric Ceramics [Haertling, 1999].

(permanent internal dipole moment) nature of the material and electrical poling process that aligns the internal dipoles of the crystallites (domains) within the ceramic and causes it to act very similar to a single crystal [Haertling, 1999], they are important not only for people to understand more about the differences between ferroelectricity and piezoelectricity in ceramic but also for applications.

Depending on the properties of ferroelectric materials, which are relatively easy with the adaption to the useful and reliable devices, the applications for ferroelectric ceramics covers nearly all areas of the daily life over the last decades. The simplicity, compact size, low cost, and high reliability of these materials triggered interests of design engineers in the whole industry.

The applications of only bulk ceramic electronic materials are ML (multilayer) capacitors, piezo-generators, piezo-motors, piezo-actuators, electrostricitve actuators, PTC (positive temperature coefficient ) sensors and so on.

Figure 1.1 is variety of ferroelectric ceramics.

## 1.2.2 Ferroelectric Film

Even the properties in the bulk form is amazing enough, people pay more attention to the thin films for fabrication of nonvolatile memories since 1960s. But the ferroelectric films were not functional before the demonstration of ferroelectric memory integrated
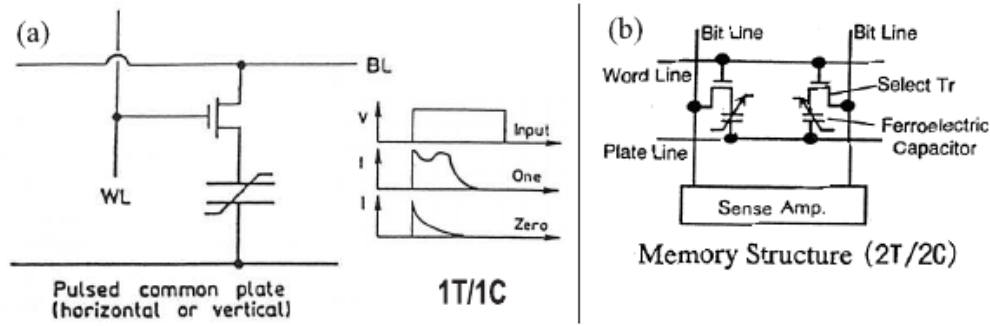
**Figure 1.2:** a)1T-1C memory design.(b) A 2T-2C memory cell in which the reference capacitor is part of the memory cell. [Dawber et al., 2005]

with silicon complementary metal-oxide semiconductor (CMOS) and the emergencies of microelectro mechanical systems (MEMS). Because portable telephones became a mass product and the introduction of polar thin films contributed since 1990s, the applications of ferroelectric thin films are mainly three domains as microsystems, memories and high frequency electrical components till now.

For the application in the field of memories, the design always use either 1 Transistor-1 Capacitor (1T/1C) or 2 Transitor-2 Capacitor (2T/2C) as figure 1.2 shows. The Samsung lead zirconate titanate based 4 Mbit 1T-1C ferroelectric memory is one of the best examples of the famous memories for commercial application, and the SEM cross-section of the device gives some indication of the complexity of design involved in a real ferroelectric memory as figure 1.3 shows [Dawber et al., 2005]. For the application in the field of semiconductor, there is an example of a ferroelectric field effect transistor (FET) device as figure 1.4.

For more information, the reader is pointed to [Dawber et al., 2005] and [Setter et al., 2006].

## 1.3 Task

The aim of the thesis is to investigate the emergence of ferroelectric property in materials of reduced dimensions. To this end the thesis performs molecular static simulations of $BaTiO_3$ thin films of varied system of number of unit cells and thickness to try to reproduce ferroelectric hysteresis loops. The number of unit cells displays the length, width and thickness of a ferroelectric thin film along x-, y- and z-direction in 3 dimensional coordinate system.
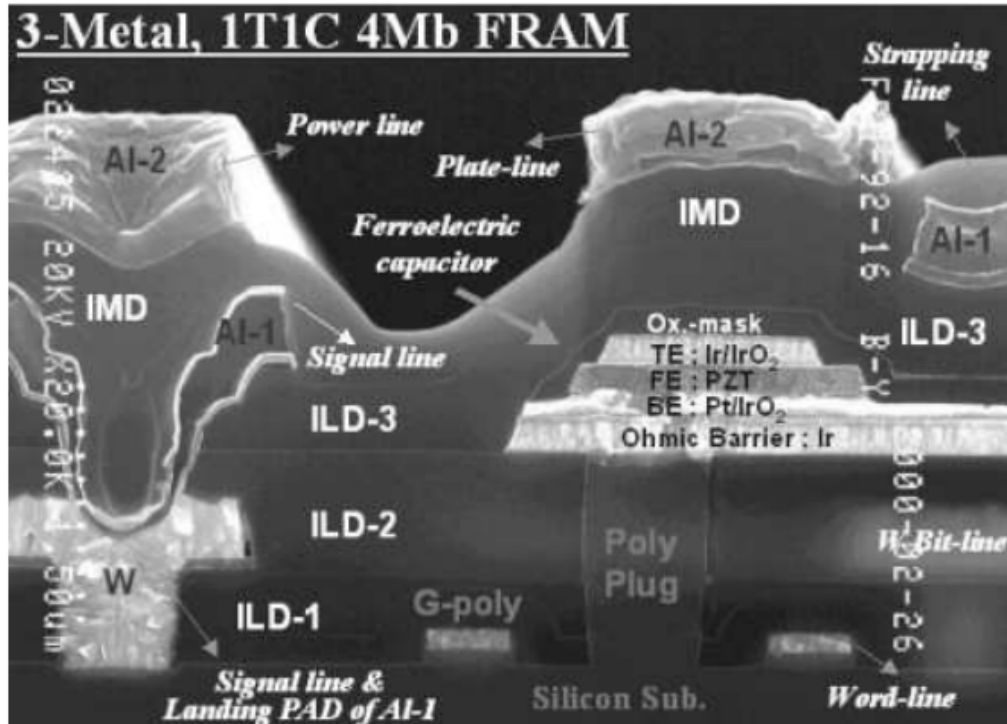
**Figure 1.3:** Cross-sectional SEM (Scanning Electron Microscope) image of the Samsung 4Mbit 1T-1C 3 metal FRAM (ferroelectric Random Access Memory) [Dawber et al., 2005].

## 1.4 Outline

The structure of the work is organized as follows. Chapter 2 introduces the basic properties of ferroelectrics and illustrates how the crystal structure enables ferroelectricity in typical perovskite structured materials. Chapter 3 introduces the model used in the simulation and the basic simulation methods. The specific methods for the simulation and the results will be shown and analyzed in Chapter 4. The last chapter mentions the conclusion and outlook of this thesis.
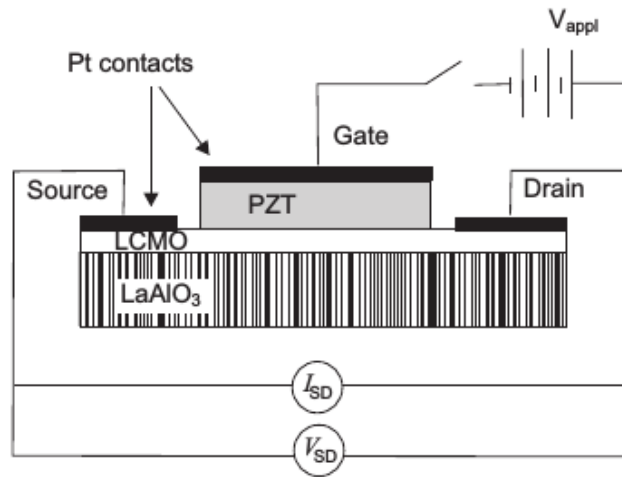
**Figure 1.4:** Schematic diagram of an all-perovskite ferroelectric FET and measurement circuit [Dawber et al., 2005].

# 2

# CRYSTAL STRUCTURE AND PROPERTIES

The investigations of ferroelectrics in thin form asked to delve into the structures and properties of the materials. It would be helpful to reduce their thickness but retain the specific characteristics for applications in the future. The significant cores to classify the ferroelectrics are the existence of spontaneous polarization and the reorientation of the polarization with the changing electric field. The topics of this chapter concern themselves with the structure and the properties of $BaTiO_3$, a typical perovskite, which is the most important and economical type of ferroelectrics.

## 2.1 Crystal Structure of Ferroelectric

As the introduction in section 1.1.1, the ferroelectrics cover a large spectrum of materials, from Rochelle salt to phosphates and arsenate of potassium and Barium titanate. These materials are divided into 4 main types according to the different unit-cell structure: the tungsten–bronze group, the oxygen octahedral group, the pyrochlore group and the bismuth layer–structure group while the vast majority of the widely used ferroelectrics are the oxygen octahedral group, also known as perovskites.

Perovskites are the materials with the same type of crystal structure as $ABO_3$, in which one of the cations, traditionally the A-ion, is the substantially largest one. The famous perovskite is $MgSiO_3$, the most abundant naturally occurring crystal structure on the

planet, because it is the major constituent of the earth's mantle [Waser and Smyth, 1996].

In order to provide a basic understanding of the nature, this part and further work will restrict themselves in this report to $BaTiO_3$ instead of other perovskites for several reasons as follows.

First, it was the earliest found ferroelectric contained neither water molecules nor hydrogen bonding, which means its structure knocked the bottom out of the previous existing hypotheses. Second, the simple crystal structure (see figure 2.1), consisting of a single stoichiometric unit makes analysis easier. The last and the most important reason is that, as one kind of a large amount of perovskites, $BaTiO_3$ shows significant electronic behaviors [Phillpot et al., 2007].
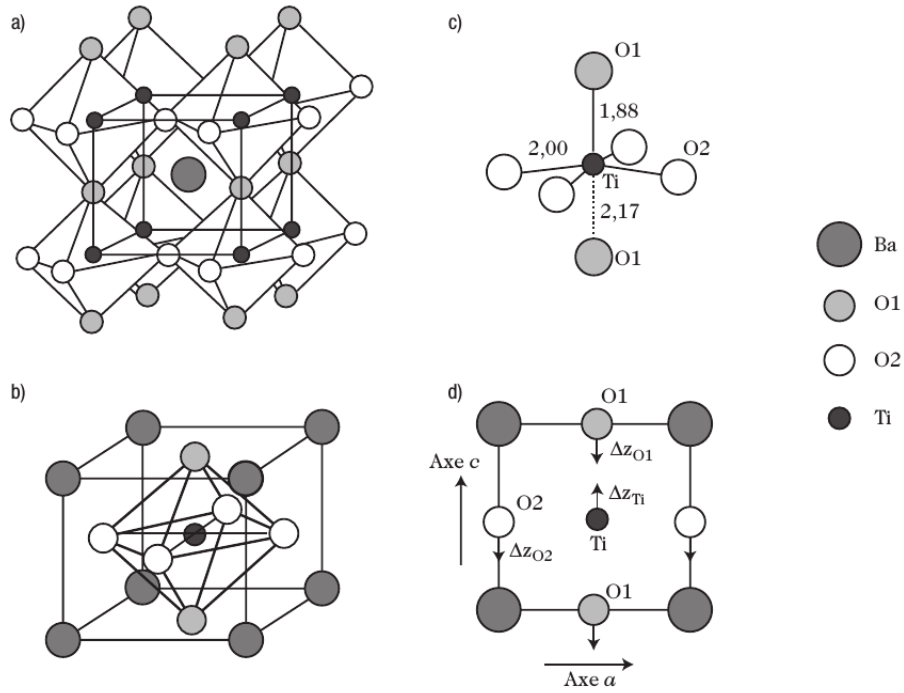


**Figure 2.1:** Undistorted, i.e., cubic, perovskite crystal structure of $BaTiO_3$ above the Curie temperature. (a) origin at a $Ba^{2+}$ ion. (b) origin at a $Ti^{4+}$ ion. (c) and (d) schematic representation of the tetragonal distortion of the latter below the Curie temperature [Niepce and Pizzagalli, 2008].

| Site | Location | Coordinates | $Z_{ion}$ |
|---|---|---|---|
| Ba cation | (2a) | $(0, 0, 0)$ | +2 |
| Ti cation | (2a) | $(\frac{1}{2}, \frac{1}{2}, \frac{1}{2})$ | +4 |
| O anion | (6b) | $(\frac{1}{2}, \frac{1}{2}, 0), (\frac{1}{2}, 0, \frac{1}{2}), (0, \frac{1}{2}, \frac{1}{2})$ | -2 |

**Table 2.1:** Atomistic positions in Cubic perovskites [Ralph, 1964].

Figure 2.1 is $BaTiO_3$, in the simplest structure – an ideal cubic perovskite with the $ABO_3$ form in a unit cell, with the Ba cations at the corners of the cube, the Ti cation in the center
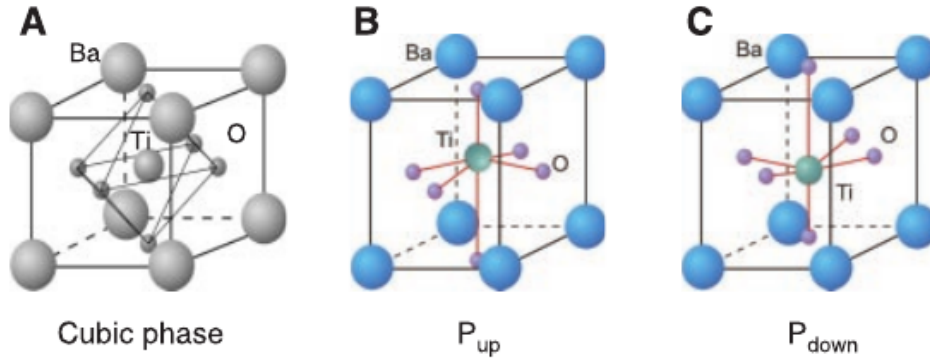
**Figure 2.2:** Structure of $BaTiO_3$. (A) cubic phase at high temperature. (paraelectric) (B) and (C) up and down polarization variants of tetragonal phases at room temperature (ferroelectric), the atomic displacements in 3-dimension [Ahn et al., 2004].

as well as the oxygen ions in the face-centered positions. Figure 2.2 shows the different atomic displacements at different temperatures, which will be talked in depth later. Table 2.1 shows the positions of the atoms for $BaTiO_3$ in details as well as table 2.2 shows the lattice constants of $BaTiO_3$ of of the cubic, tetragonal, orthorhombic, and rhombohedral phases with empirical results and theoretical ones.

## 2.2 Basic Properties

As former introductions, there are 2 basic properties in ferroelectrics, one is the spontaneous polarization and the other one is the reorientation of the polarizations for changing external electric field. Others properties are the experimental phenomena.

### 2.2.1 Polarization

The name of ferroelectric materials, which can be made an analogy with ferromagnetic, is given to present the two basic properties above, where they are both mentioning "polarization". That is why the polarization is the core of the physics of ferroelectrics.

The term "polarization" in macroscopic view is a very principle definition for the dielectric media. It simply segues into a vector which means electric dipole moment per unit volume in macroscopic.

For the polarization of the ferroelectric, the definition of electric dipole element need to be introduced. It is induced as the response of systems to external electric fields. For the finite ferroelectric crystal material, the locations of the barycenters of anions and cations are not overlapped, which means the electric dipole moment $d$ should be generated as

| Phase | Lattice Constant a(Å), $\alpha$ (°) | | | Method |
|-------|------|------|------|--------|
| Cubic | 4.000 | | | DFT(LDA) |
| | 4.000 | | | Experiment |
| | 4.030 | | | Theory |
| | 4.006 | | | Theory |
| | 3.943 | | | Theory |
| Tetragonal | a (Å) | | c(Å) | |
| | 3.996 | | 4.035 | DFT(LDA) |
| | 3.992 | | 4.036 | Experiment |
| | 3.943 | | 3.994 | Theory |
| Orthorhombic | a (Å) | b (Å) | c(Å) | |
| | 5.704 | 3.963 | 5.683 | DFT(LDA) |
| | 5.682 | 3.990 | 5.669 | Experiment |
| Rhombohedral | a (Å) | | $\alpha$(°) | |
| | 4.000 | | 89°56' | DFT(LDA) |
| | 3.998 | | 89°52.5' | Experiment |
| | 4.000 | | 89°54' | Experiment |
| | 4.000 | | 89°51' | Theory |

**Table 2.2:** The relaxed structures of $BaTiO_3$ of the cubic, tetragonal, orthorhombic, and rhombohedral phases with the experimental data and theoretical results [Wang et al., 2010].

follow:

$$\mathbf{d} = \sum_i q_i \mathbf{r_i} \tag{2.1}$$

where the charge of the $i^{th}$ particle is $q_i$ and the location of $i^{th}$ particle is $r_i$.

For the definition given above, polarization is the result of electric dipole element per unit volume. Then the formula of the total polarization of a single unit cell is as follow:

$$\mathbf{P} = \frac{1}{V} \sum_i^N q_i \mathbf{r_i} \tag{2.2}$$

where N is the total numbers of the charges and V is the volume of the unit cell.

The complex behavior happens for the combination of ionic and electronic polarization for the ferroelectrics. Even Berry phase and Warrier wave function is better to calculate the polarization according to the modern theory [Resta, 1997], a new tensor named Born effective charges as a very important physical quantity for ferroelectric in the theory for lattice dynamics was introduced to estimate the polarization by the displacements of ions.

The change of polarization for the simple classical electrostatic point charge can be cal-
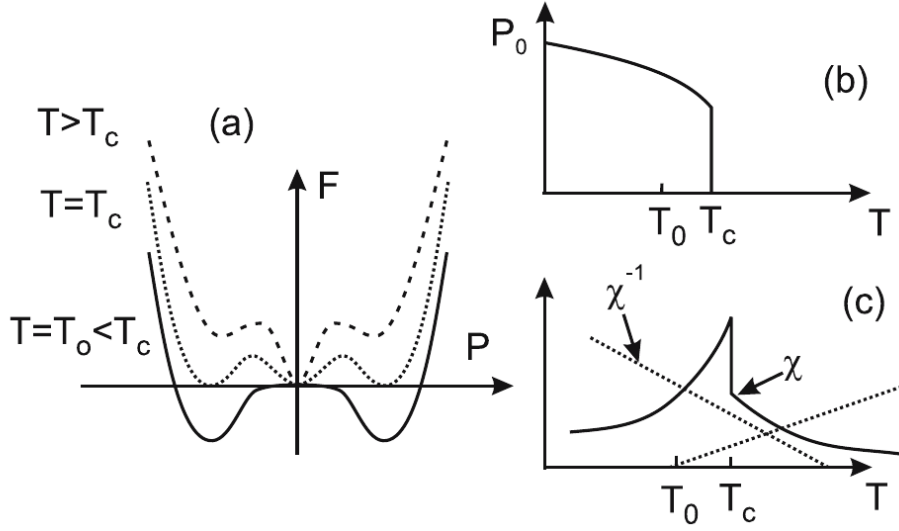
**Figure 2.3:** First-order phase transition. (a) free energy as a function of the polarization at T > $T_0$ , T = $T_0$ , and T < $T_0$ ;(b) spontaneous polarization $P_0$(T) along changing temperature; (c) the susceptibility $\chi$ and its inverse, where $\chi = \frac{\partial P}{\partial E}|_{P_0}$ is evaluated at the equilibrium polarization $P_0(T)$ [Rabe et al., 2007].

culated with Born effective charges as follow:

$$\delta \mathbf{P} = \frac{|e|}{V} \sum_{m=1}^{N} \mathbf{Z_i} \cdot \delta \mathbf{r_i} \qquad (2.3)$$

where $e$ is the electronic charge, $V$ is the volume of the unit cell, $N$ is the total number of the ions, $r_i$ is the displacement (vector) of the $i^{th}$ atom and $Z_i$ are the Born effective charge tensor of the $i^{th}$ atom while the sums run over both anions and cations in the unit cell. The second order of Born effective charge of the $i_{th}$ can be describe as [Endres and Steinmann, 2015]:

$$\vec{Z}_i = \begin{pmatrix} Z_{11} & Z_{12} & Z_{13} \\ Z_{21} & Z_{22} & Z_{23} \\ Z_{31} & Z_{32} & Z_{33} \end{pmatrix} \qquad (2.4)$$

Table 2.3 shows the different Born effective changes $Z^*$ of $BaTiO_3$ in cubic structure calculated by different methods like local density approximation (LDA) in density functional theory (DFT) for linear response (the first row) and Berry phase (the second row), pseudopotential self-interaction correction (Pseudo-SIC) and experiment.

The one of the important definitions is spontaneous polarization, the equilibrium value of switchable polarization **P**, which is caused by the electric dipole moment with the shifting of off-center Ba or Ti or both cations as figure 2.1 and 2.2 show. The crystal structure with a polar space group also has the nonzero spontaneous polarization. The spontaneous

polarization in all three directions in space during the experiment or the simulation can be calculated as $P_S = ||\mathbf{P_S}|| = \sqrt{P_{S,x}^2 + P_{S,y}^2 + P_{S,z}^2}$ [Endres and Steinmann, 2015]. For ferroelectric state, it can be accurately calculated from the Berry-phase formalism or estimated with the formula above because the Born effective charges are sensitive to the displacements of ions. The spontaneous and switchable polarizations that can therefor be used for data storage [Rabe et al., 2007].

The other one is remanent polarization, which means the material will remain polarized and the polarization will be a certain value when the strength of electric field is changed to be zero.

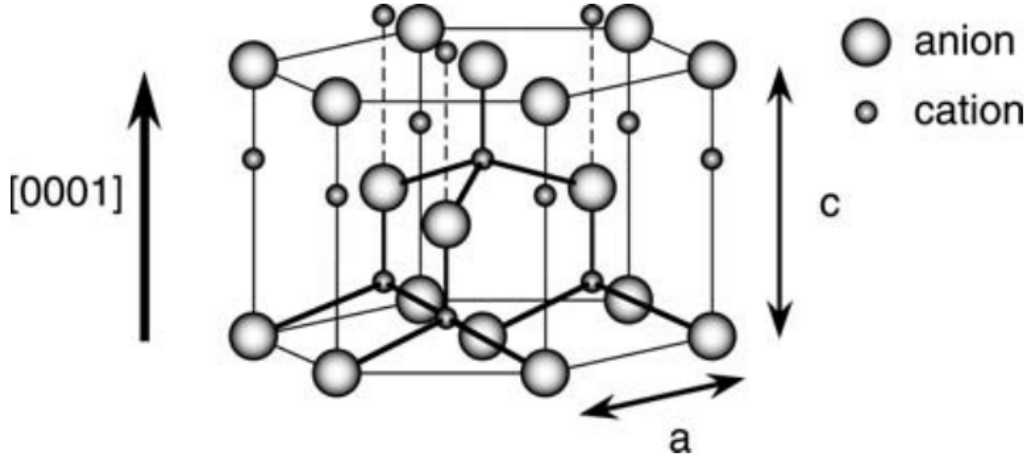## 2.2.2 Hysteresis Loop



**Figure 2.4:** Example of the structure of the material has spontaneous polarization but is not ferro-electric [Rabe et al., 2007].

There are materials which can display the spontaneous polarization but do not switch with the changing external electric field, as ZnO and GaN. The structure can be as above.

| $Z_A^*$ | $Z_B^*$ | $Z_{O\parallel}^*$ | $Z_{O\perp}^*$ | $\frac{Z_A^*}{Z_A}$ | $\frac{Z_B^*}{Z_B}$ | Method | Reference |
|---|---|---|---|---|---|---|---|
| 2.77 | 7.25 | -5.71 | 2.15 | 1.39 | 1.81 | DFT(LDA) | [Ghosez et al., 1998] |
| 2.75 | 7.16 | -5.69 | -2.11 | 1.38 | 1.79 | DFT(LDA) | [Zhong et al., 1994] |
| 2.61 | 5.88 | -4.43 | -2.03 | 1.31 | 1.47 | Pseudo-SIC | [Filippetti and Spaldin, 2003] |
| 1.63 | 7.51 | -2.71 | -3.72 | 0.82 | 1.88 | Shell Model | [Ghosez et al., 1995] |
| 2.9 | 6.7 | -4.8 | -2.4 | 1.45 | 1.68 | Experiment | [Axe, 1967] |

**Table 2.3:** Born effective charges of various $BaTiO_3$ compounds in their cubic structure while $Z_A$ and $Z_B$ are the nominal ionic charges for atom Ba and Ti.(adapted from [Ghosez et al., 1998])
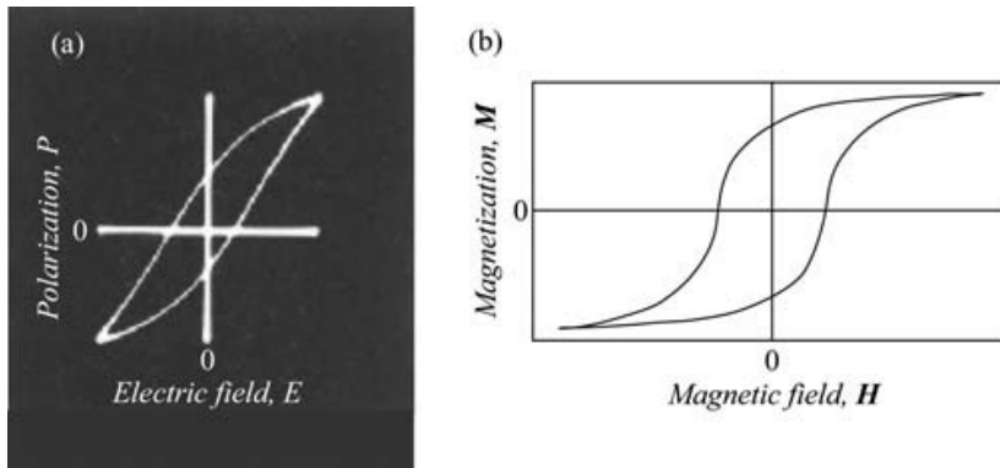
**Figure 2.5:** Hysteresis loops in (a) $BaTiO_3$ whose cubic structure is introduced in section 2.1, and (b) $Fe$, a ferromagnetical material [Rabe et al., 2007].
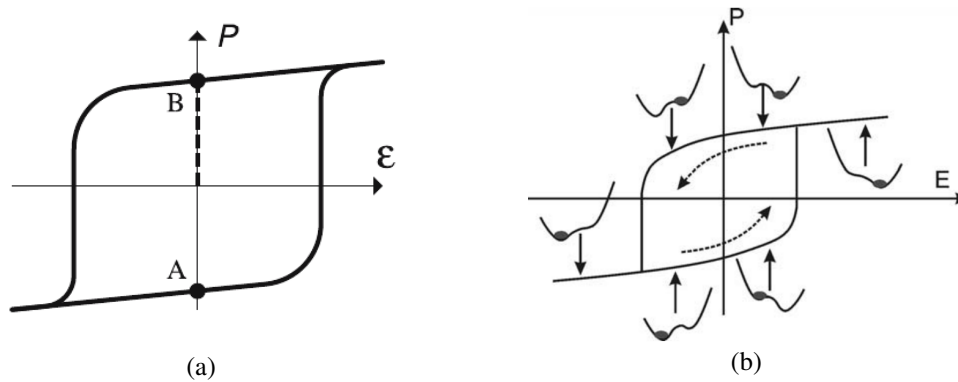


**Figure 2.6:** Schematic picture of hysteresis in an idealized ferroelectric [Rabe et al., 2007].

Ferroelectric was named as "ferro-" is a misnomer for it can not consist of iron cations. The reason for the name is the first investigations in Rochelle salt, the primal ferroelectric in the world, found the electric hysteresis like the magnetic one of iron. The comparison between hysteresis loop for ferroelectric – $BaTiO_3$ and for ferromagnetical material – $Fe$ is shown in figure 2.5.

The behavior of hysteresis loop is essential not only for the judgment of ferroelectric itself but also for the storage application where the orientation of the polarization for either electric hysteresis or magnetic one can be marked as "0" or "1" for the single binary value – data bit.

The hysteresis circle can also be utilized to measure the magnitude of the spontaneous polarization. As figure 2.6 (a) shows, the magnitude of spontaneous polarization $P_S$ for the transition from the left to the right enantiomorphous ferroelectric of $ABO_3$ tetragonal

structure in figure 2.7 can be defined as:

$$P_S = \frac{1}{2}(P_B - P_A) \tag{2.5}$$

In the empirical measurements, the aim of the magnitude is neither $P_A$ nor $P_B$ but their difference as $\triangle P$ (vertical dashed segment along P-direction in figure 2.6 (a)).

Figure 2.6 (b) shows the one calculated with Landau-Devonshire theory where all the dipoles will be reversal to reorientate the polarization.
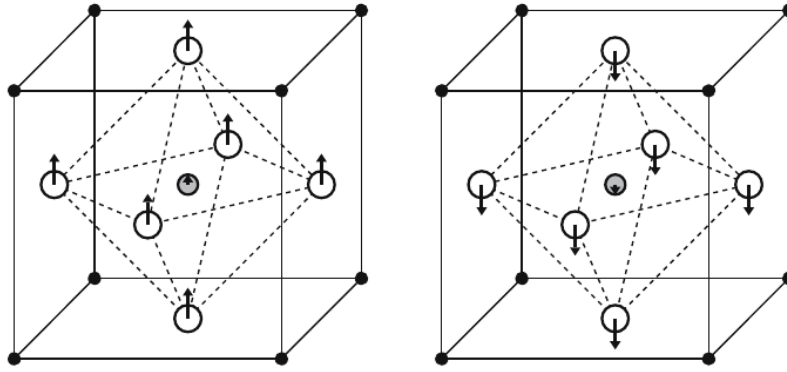


**Figure 2.7:** Two enantiomorphous $ABO_3$ tetragonal structure with polarization along [001] applied by the electric field [Rabe et al., 2007].

## 2.2.3 Other Important Phenomena

### Phase Transition

The crystal phase transition will occurs for several reasons such as temperature, pressure and so on. Landau first found the magnetic phase transition, but Landau theory can be only described in macroscopic. The Landau-Denvonshire theory and Landau-Ginzburg theory were introduced later and can be used to discuss the different ferroelectrics as follows.

| Phenomenology | Ferroelectric (near Tc) |
|---|---|
| Landau–Devonshire theory (uniform polarization) | Poled bulk system |
| Landau–Ginzburg theory (polarization with spatial gradient) | Bulk system |
| Landau–Ginzburg theory with boundary conditions | Film |

**Table 2.4:** Phenomenologies and relevant ferroelectric systems (close to Tc) [Rabe et al., 2007].

Tinte et al. presented the results simulated by molecular dynamics method (MD) for a (001) $TiO_2$-terminated stress-free slab of 28 Å width [Tinte and Stachiotti, 2001] as

figure 2.8, where $P_x$ and $P_y$ (polarizations in x- and y-direction separately) show the phase transitions with increasing temperature.
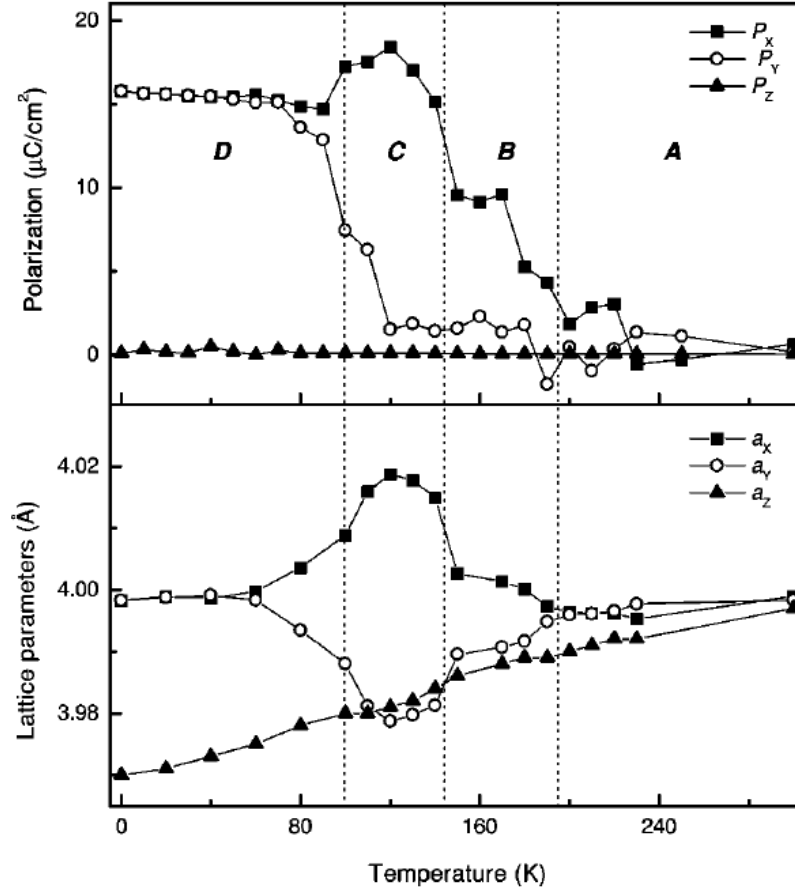


**Figure 2.8:** Phase transitions of the $BaTiO3$ film with molecular dynamics method (upper panel: average polarization in three directions; lower panel: corresponding cell parameters) [Tinte and Stachiotti, 2001].

Figure 2.9 shows the phase transitions of a (001)-oriented $BaTiO_3$ film under a symmetrical biaxial constraint, where $T^P$ means tetragonal paraelectric phase, $T^F$ means tetragonal ferroelectric phase, $O^F$ means orthogonal ferroelectric phase and $M^F$ means monoclinic ferroelectric phase. Table 2.5 presents the magnitude of the spontaneous polarizations and the Curie temperature of $BaTiO_3$ with the phase transition. It is obvious that the transition temperatures have large relative errors for both methods which could generate phase transitions successfully comparing with the one investigated by the experiment.

## Size Effect

The size effect of the ferroelectrics becomes more and more significant in recent twenty years, because the smaller the film is, the more data can be stored in the same volume. The
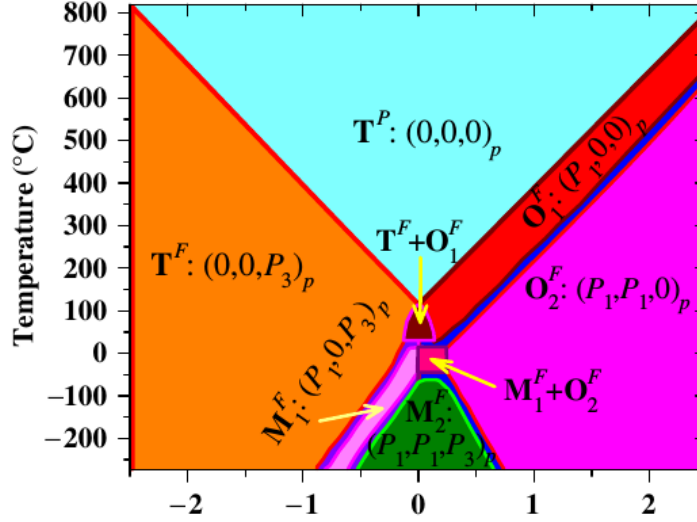
**Figure 2.9:** $BaTiO_3$ Films in different phases with the function of temperature and substrate constraint strain [Chen, 2008].

| Approach | | Experiment | Heff | | Shell Model |
|---|---|---|---|---|---|
| Cubic | $P_s$ | 0 | 0 | 0 | 0 |
| ↓ | $T_c$ | 403 | 335 | 297 | 190 |
| Tetragonal | $P_s$ | 27 | 30 | 28 | 17 |
| ↓ | $T_c$ | 278 | 240 | 230 | 120 |
| Orthorhombic | $P_s$ | 36 | 37 | 35 | 14 |
| ↓ | $T_c$ | 183 | 190 | 200 | 90 |
| Rhombohedral | $P_s$ | 33 | 45 | 43 | 12.5 |

**Table 2.5:** Magnitude of the spontaneous polarizations (Ps, $\mu C/cm^2$ ) and Curie temperatures (Tc, in K) of $BaTiO_3$ as predicted by an effective Hamiltonian (Heff) and a shell-model approach [Rabe et al., 2007].

thickness of the ferroelectric film is reduced with the developments of the experiments and theories as section 1.1.2 describes. And studying the growth of epitaxial thin films is the best way to access the size effect nowadays [Rabe et al., 2007].

The first-principles calculations for ferroelectric materials with the assistance of computational simulations also help a lot in this field. Chapter 5 will discuss it in details.

# 3

# SIMULATION METHODS

The simulation methods have emerged to investigate the properties of ferroelectrics as an aid with the burgeoning development of computer for last two decades. This chapter illustrates the fundamental methods based on the ferroelectric crystal structures and quantum mechanics.

## 3.1 Atomistic Model

All matter is made up of atoms. Then the atomistic modeling are essential to understand materials, which means the motion of every atom can be sketched in microscopy. The construction of atomistic model is the first step for the molecular simulation.

### 3.1.1 Effective Hamiltonian Approaches

The effective Hamiltonian is an approach generated by the Taylor expansion of the energy around the high-symmetry paraelectric phase in terms of the soft-mode degrees of freedom and the homogeneous strain [Rabe et al., 2007], which means it asked the soft-mode amplitude by the constant factor.
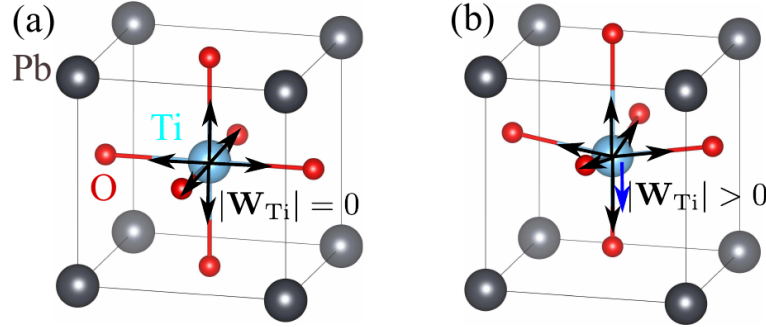
## 3.1.2 Bond-valence Model



**Figure 3.1:** Schematic representation of bond-valence vector summation around $T_i$ in (a) cubic $PbTiO_3$ and (b) tetragonal $PbTiO_3$. The black arrows scale the individual bond-valences, and the blue arrow shows the resultant bond-valence vector sum $W_{T_i}$. [Shin et al., 2005]

Compared with the effective Hamiltonian approaches, bond-valence models have simpler forms. The bond-valence theory assumes the valence of an atom is distributed among the bonds it forms, and the bond valences (or bond orders) are correlated with the bond length through an inverse power relation, with the total atomic valence of each atom equal to the sum of its bond valences [Shin et al., 2005]. As a potential model, it will be helpful to simulate the large supercells systems at nonzero temperatures and electric fields. Figure 3.1 and 3.2 shows the schematic representation of bond-valence vector summation at $T_i$ of $PbTiO_3$ in different phases and the angle potential.

The total energy equation of bond-valence model $E_{BV}$ can be described as:

$$E_{BV} = E_b + E_{coulomb} + E_r + E_{angle}, \tag{3.1}$$

where $E_b$ is the bond-valence potential energy, $E_{coulomb}$ is the Coulomb potential energy, $E_r$ is the repulsive potential energy and $E_{angle}$ is the angle potential energy.
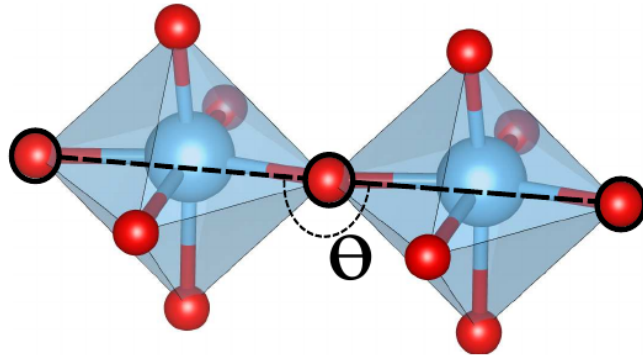


**Figure 3.2:** Angle potential in bond-valence mode [Shin et al., 2005].

### 3.1.3 Core-shell Model

The core-shell model, on the basis of effective Hamiltonian, has a broad application of the simulation of materials, including ferroelectric ones because it can describe the deformation of the electronic structure of an atom owing to the interactions with other neighbor ones via the potential energy function assuming an equilibrium separation of zero [Dove, 2008, Sang et al., 2008].

In this model, every atom is divided into two parts, the inner massive core with positive charge numbered as odd whereas the outer massless shell with negative charge numbered as even.
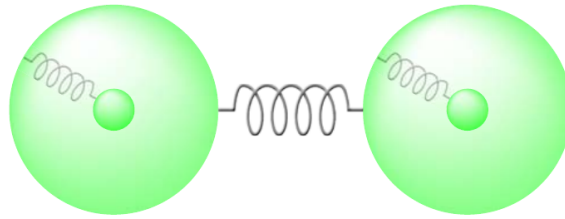


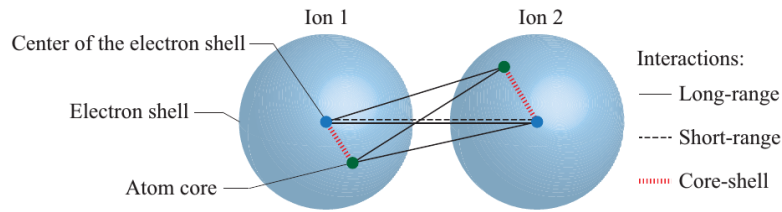**Figure 3.3:** Schematic of core-shell model [Dove, 2008].



**Figure 3.4:** Interactions between two ions using the core-shell model [Endres and Steinmann, 2015].

Figure 3.3 illustrates the schematic of harmonics core-shell model and figure 3.4 shows three different interactions between two atoms which will be used in the simulation.

The harmonic connection in a core-shell model can be described as:

$$V(\omega) = \frac{1}{2k_2}\omega^2 \tag{3.2}$$

where the $\omega$ is the relative distance between the core and shell in the same ion as well as $k_2$ is the potential parameter. And the anharmonic one is:

$$V(\omega) = \frac{1}{2k_2}\omega^2 + \frac{1}{24k_4}\omega^4 \tag{3.3}$$

where $k_4$ is another potential parameter. The core-shell model can be either isotropic or

anisotropic in the simulations.

Besides core-shell model and bond-valence model, Carter-Goddard-Malrieu-Trinquier model is also a famous potential model.

### 3.1.4 Different Interactions Based on Core-shell Model

The interactions between different atoms are considered as the sum of the long-range electrostatic ones between any two particles and the short-range ones between any two electron shells of different atoms in the simulation, their potentials can be described as follow in general:

$$V(\mathbf{r_{ij}}) = V_{long-range}(\mathbf{r_{ij}}) + V_{short-range}(\mathbf{r_{ij}})$$
$$\mathbf{r_{ij}} = \mathbf{r_i} - \mathbf{r_j}$$

(3.4)

where $\mathbf{r_{ij}}$ is the relative distance between $i^{th}$ and $j^{th}$ particle with charges $q_i$ and $q_j$ separately.

When the Coulomb interaction is utilized as the long-range interaction, $V_{long-range}(\mathbf{r_{ij}})$ can be described as $V_{ij}^{Coulomb}$:

$$V_{ij}^{Coulomb} = \frac{q_i q_j}{4\pi\varepsilon_0 |\mathbf{r_{ij}}|},$$

(3.5)

where $\varepsilon_0$ is vacuum permittivity, the value of the absolute dielectric permittivity of classical vacuum.

The short-range interaction is represented by either Buckingham potential:

$$V_{ij}^{Buck} = A \cdot exp\left(-\frac{|\mathbf{r_{ij}}|}{\rho} - \frac{C}{(|\mathbf{r_{ij}}|)^6}\right)$$

(3.6)

or Rydberg potential:

$$V_{ij}^{Ryd} = (A + B \cdot |\mathbf{r_{ij}}|)exp\left(-\frac{|\mathbf{r_{ij}}|}{\rho}\right),$$

(3.7)

where A, $\rho$, C are the potential parameters.

The Buckingham potential is chosen for the simulation in this work.

The long-range potential described by Coulomb law decreases slowly with the increasing distances between ions with $\mathbf{r_{ij}}^{-1}$ as equation (3.5) shows. The computation of its interaction is expensive significantly since the indispensable cut-off radius is asked for the accuracy in the simulations. The stability shows the Coulomb potential does not approach zero, that is why there is jumps in the total potential energy at the cut-off radius $R_c$ [Endres and Steinmann, 2015]. The Wolf summation, a damping algorithm, can solve

this problem:

$$\Phi_i^{Wolf} = \frac{1}{4\pi\varepsilon_0} \sum_{\substack{j>i \\ |\mathbf{r_{ij}}|<R_c}} \left[ \frac{q_i q_j erfc(\alpha \cdot |\mathbf{r_{ij}}|)}{|\mathbf{r_{ij}}|} - \lim_{|\mathbf{r_{ij}}| \to R_c} \left( \frac{q_i q_j erfc(\alpha \cdot |\mathbf{r_{ij}}|)}{|\mathbf{r_{ij}}|} \right) \right]$$
$$- \frac{1}{2} \left( \frac{erfc(\alpha \cdot R_c)}{2R_c} + \frac{\alpha}{\pi^{\frac{1}{2}}} \right) \sum_{i=1}^{N} q_i^2 \quad , \tag{3.8}$$

where $erfc(\cdot)$ is the complementary error function as:

$$erfc(x) = 1 - \frac{2}{\pi^{\frac{1}{2}}} \int_0^x e^{-\tau^2} d\tau \quad , \tag{3.9}$$

in which $\alpha$ is the potential damping factor.

Another two additional requirements for the Wolf summation technique need to be paid attention to. One is the accurate simulation for the Coulomb interaction asks the damping parameter $\alpha$ small enough, the other one is to choose the cut-off radius $R_c$ large enough even though the larger one will cost more expensive. There are others algorithms which can also solve the problem like Ewald summation, but the Wolf summation is introduced here for the simulation.

All of the equations in section 3.1.3 are from [Endres and Steinmann, 2015].

| Atom | Core Charge | Shell Charge | $k_2$ | $k_4$ |
|------|-------------|--------------|-------|-------|
| Ba | 5.62 | -3.76 | 251.8 | 0.0 |
| Ti | 4.76 | -1.58 | 322.0 | 500.0 |
| O | 0.91 | -2.59 | 31.0 | 4000.0 |

| Short Range | A | $\rho$ | C |
|-------------|---|--------|---|
| Ba-O | 1061.30 | 0.3740 | 0.0 |
| Ti-O | 3769.93 | 0.2589 | 0.0 |
| O-O | 4740.00 | 0.2686 | 160.0 |

**Table 3.1:** Parameters for core-shell model potentials of $BaTiO_3$ in the simulation [Sepliarsky et al., 2005]

The core-shell model parameters of $BaTiO_3$ used in the simulation is in table 3.1. The charge is determined from charge neutrality. The relative distance between the core and the shell of the positive particles is small enough to neglect the van der Waals interaction of positive particles to the oxygen atoms and the shell model energy.

## 3.1.5 Total Model in the Simulation

In the simulation, the boundary condition in x- and y-direction are periodic as well as the one in z-direction is shrink-wrapped.
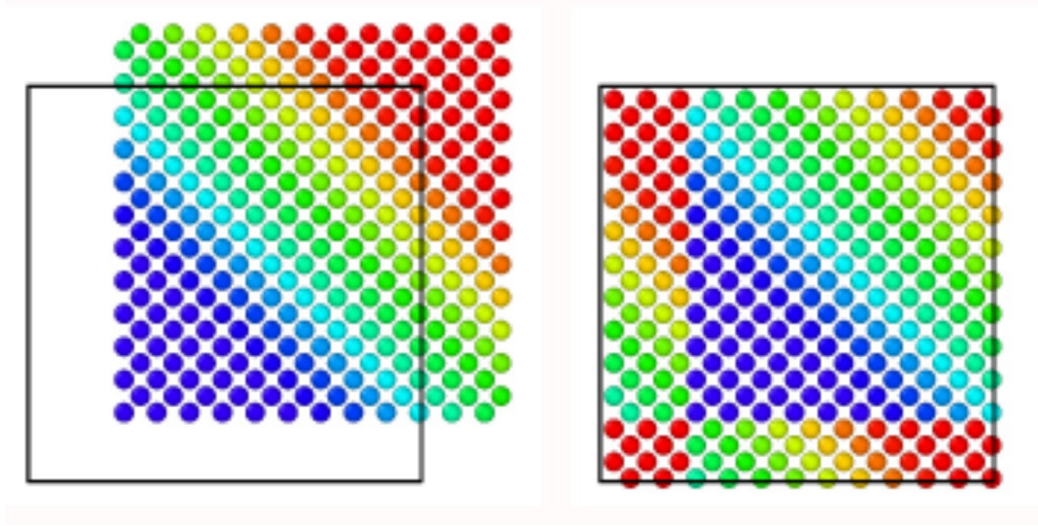
**Periodic Boundary Condition**



**Figure 3.5:** Scheme of periodic boundary condition and related part of shrink-wrapped boundry condition [Stukowski, 2009].

Considering a partial differential equation as: $v_t + av_x = 0 \quad x \in (0,1)$, along with the initial condition $v(x,0) = f(x) \quad x \in [0,1]$, the periodic boundary condition means $v(0,t) = v(1,t)$ [Thomas, 2013]. The left one on figure 3.5 shows a cell with the boundary (the black box). Which means that, if there are some atoms which are going out of one side of the boundary as the left figure, the periodic boundary condition makes sure those escaping atoms will reappear on the opposite as the right figure shows.

**Shrink-wrapped Boundary Condition**

If there are the unit cells generated as the left one on figure 3.5, some or all of the unit cells in the system are not in the given boundary, the shrink-wrapped boundary condition means the box size will adjust to fit the bounds of atoms, no matter where they are moving to, instead of what the right one on figure 3.5. It is a kind of free-energy boundary condition which can avoid atoms leaving from the simulation box.

The model of unit cells is generated by Moltemplate. Because of the different boundary conditions in different directions, the simulation sets the model in xy-plane like figure 3.6(c) while the l is the number of unit cells in x- and y-direction. In xz- and zy-direction, the model is as figure 3.6(d). The different set is in z-direction. There is a gap between any two unit cell in z-direction and the width $d$ is the lattice parameter $a$. All of the parameters of the $BaTiO_3$ in the core-shell model used in the simulation are as table 3.1 and all of the lattice constants are in table 2.2.
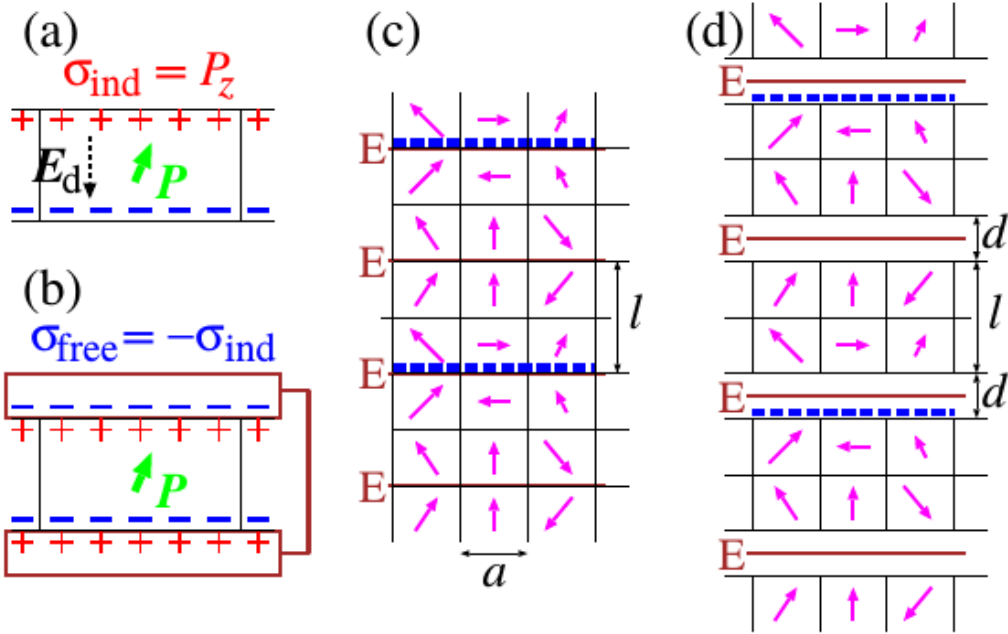
**Figure 3.6:** Schematic illustrations of ferroelectric thin films of thickness $l$ unit cells. (a) isolated thin film in vacuum. (b) thin film sandwiched between short-circuited perfect electrodes. (c) the model in xy-plane. (d) the model in xz- or yz-plane. [Nishimatsu et al., 2008]

## 3.2 Simulation Methods

There are several basic methods to investigate the properties of ground-state atoms, such as molecular statics or dynamics method and Monte Carlo method. The molecular statics and dynamics method are deterministic simulation methods as well as Monte Carlo method relies on the repeated random data to get the result.

### 3.2.1 Molecular Statics

The molecular statics neglects the motions of the electrons and constructs function by the external force field to describe the relationship between the locations of cores of the ions and the energy according to Born-Oppenheimer approximation. The parameters used in this method can be calculated by the quantum mechanics or generated from the experiments. There are three advantages. First, it can calculate the system with large supercells containing thousands of unit cells. Second, it calculates rapidly. The last one is its results are relative approximate to the real one under some certain circumstances.

The theory of molecular statics is generated from the minimization of the total potential energy in a system while the discrete particle system is analogous to the one-dimensional nonlinear finite elements [Endres and Steinmann, 2015]. Therefore, the total potential

energy of a discrete particle system can be described as a sum of internal and external potential energies as follow:

$$E^{tot} = \Phi^{int}(\mathbf{r}) + \Phi^{ext}(\mathbf{r})$$
$$= \frac{1}{2} \sum_{i=1}^{N} \sum_{j \neq i}^{N} \Phi^{int}(\mathbf{r_{ij}}) + \sum_{i=1}^{N} \mathbf{f_i^{ext}} \mathbf{r_i} \qquad , \qquad (3.10)$$

where N is the number of particles and the $\mathbf{r_i}$ is the position of the $i^{th}$ particle and $\mathbf{r_{ij}}$ is the distance vector between the $i^{th}$ and the $j^{th}$ particle as equation (3.3), $\mathbf{f_i^{ext}}$ is the forces caused by the external conservative fields like electric field (the work used in the simulation). The external electric force on the $i^{th}$ particle can be calculated as:

$$\mathbf{f_i^{ext}} = e_i \cdot q_i, \qquad (3.11)$$

where $e_i$ is strength of the external electric field at the coordinate the $i^{th}$ particle locates and $q_i$ is the charge of the $i^{th}$ particle. Then the minimization of the total potential energy can be calculated for the mechanical equilibrium as:

$$\frac{\partial E^{tot}}{\partial \mathbf{r}} = 0, \qquad (3.12)$$

which means the residual $\mathbf{f}(\mathbf{r})$ is zero as equation (3.12).

$$\mathbf{f}(\mathbf{r}) = \mathbf{f^{ext}}(\mathbf{r}) - \mathbf{f^{int}}(\mathbf{r}) \qquad (3.13)$$

Assuming the force is linear with stiffness coefficient $K$, then

$$\mathbf{f}(\mathbf{r}) = K \cdot d\mathbf{r}, \qquad (3.14)$$

The interaction between any two atoms in the system can be described as the one-dimensional truss nonlinear element in finite elements. [Endres and Steinmann, 2015], which means the local internal force and local stiffness matrix between ever two atoms can be calculated as:

$$\mathbf{f_{ij}} := \frac{\partial \Phi_{ij}}{\partial \mathbf{r_{ij}}}$$
$$\mathbf{K_{ij}} := \frac{\partial^2 \Phi_{ij}}{\partial \mathbf{r_{ij}}^2} \qquad (3.15)$$

where $\Phi_{ij}$ is the interaction potential energy of the relative position of $i^{th}$ and $j^{th}$ atoms.

The interaction between any two ions, as long-range interaction introduced in section 3.1.2, is described by the Coulomb law with Wolf summation, and the equations in the

discrete particle system are:

$$\mathbf{f_{ij}^{Wolf}} = \frac{\partial \Phi_{ij}^{Wolf}}{\partial \mathbf{r_{ij}}} = \frac{q_i \cdot q_j}{4\pi\varepsilon_0} \left[ erfc(\alpha|\mathbf{r_{ij}}|) \frac{\mathbf{r_{ij}}}{|\mathbf{r_{ij}}|^3} + \frac{2\alpha}{\pi^{\frac{1}{2}}} exp(-\alpha^2|\mathbf{r_{ij}}| \frac{\mathbf{r_{ij}}}{|\mathbf{r_{ij}}|^2}) \right.$$
$$\left. - erfc(\alpha R_c) \frac{\mathbf{r_{ij}}}{R_c^3} - \frac{2\alpha}{\pi^{\frac{1}{2}} exp(-\alpha^2 R_c^2) \frac{\mathbf{r_{ij}}}{R_c^2}} \right] \tag{3.16}$$

$$\mathbf{K_{ij}^{Wolf}} = \frac{\partial^2 \Phi_{ij}^{Wolf}}{\partial \mathbf{r_{ij}}^2} = \left[ erfc(\alpha|\mathbf{r_{ij}}|) \frac{1}{|\mathbf{r_{ij}}|^3} \left[ \mathbf{I} - \frac{3}{|\mathbf{r_{ij}}|} \mathbf{r_{ij}} \otimes \mathbf{r_{ij}} \right] - \frac{2\alpha}{\pi^{\frac{1}{2}}} exp(-\alpha^2|\mathbf{r_{ij}}|^2) \frac{1}{|\mathbf{r_{ij}}|^4} \mathbf{r_{ij}} \otimes \mathbf{r_{ij}} \right.$$
$$+ \frac{2\alpha}{\pi^{\frac{1}{2}}} exp(-\alpha^2|\mathbf{r_{ij}}|^2) \left[ \mathbf{I} - \frac{2}{|\mathbf{r_{ij}}|^2 \mathbf{r_{ij}} \otimes \mathbf{r_{ij}}} \right]$$
$$- \frac{4\alpha}{\pi^{\frac{1}{2}}} exp(-\alpha^2|\mathbf{r_{ij}}|^2) \frac{1}{|\mathbf{r_{ij}}|^2} \mathbf{r_{ij}} \otimes \mathbf{r_{ij}}$$
$$\left. - erfc(\alpha R_c) \frac{1}{R_c^3} \mathbf{I} - \frac{2\alpha}{\pi^{\frac{1}{2}}} exp(-\alpha^2 R_c^2) \frac{1}{R_c^2} \mathbf{I} \right] \tag{3.17}$$

As well as the interaction between shells of any two ions, as short-range interaction described by Buckingham potential, can be written as:

$$\mathbf{f_{ij}^{Buck}} = \frac{\partial \Phi_{ij}^{Buck}}{\partial \mathbf{r_{ij}}} = -\frac{A}{\rho} exp\left( -\frac{|\mathbf{r_{ij}}|}{\rho} \right) \frac{\mathbf{r_{ij}}}{|\mathbf{r_{ij}}|} + 6C \frac{\mathbf{r_{ij}}}{|\mathbf{r_{ij}}|^8} \tag{3.18}$$

$$\mathbf{K_{ij}^{Buck}} = \frac{\partial^2 \Phi_{ij}^{Buck}}{\partial \mathbf{r_{ij}}^2} = -\frac{A}{\rho|\mathbf{r_{ij}}|} exp\left( -\frac{|\mathbf{r_{ij}}|}{\rho} \right) \left[ \frac{1}{\rho|\mathbf{r_{ij}}|} + \frac{1}{|\mathbf{r_{ij}}|^2 \mathbf{r_{ij}} \otimes \mathbf{r_{ij}} - \mathbf{I}} \right]$$
$$+ 6C \frac{\mathbf{r_{ij}}}{|\mathbf{r_{ij}}|^8} \left[ \mathbf{I} - 8\frac{1}{|\mathbf{r_{ij}}|^2} \mathbf{r_{ij}} \otimes \mathbf{r_{ij}} \right] \tag{3.19}$$

Equation (3.15) and (3.16) shows the partial derivatives of Wolf summation technique for the improvement of stability cost really expensive than the classical Coulomb potential does as equation (3.4), because the reorientation of polarizations with changing external electric field need the stability and Wolf summation is indispensable in this part [Endres and Steinmann, 2015]. The disadvantage of the molecular statics is its results contain no dynamic properties of the simulated systems.

## 3.2.2 Molecular Dynamics

Molecular dynamics, generated from the basics of Newton's law and molecular mechanics, has been utilized extensively to solve the problems with a large scale sampling. The time-dependent dynamical and thermal properties at high temperature can be obtained unambiguously with this method. The fundamentals of this method are the conservation of energy and momentum. The steps of MD method are introduced briefly in this part.

### Foundation

First of all, considering a system of N particles obeying classical mechanics in the three dimensional coordinates, the energy of the system is the summation of the potential and kinetic energy of all the particles, which means the work between any two points $A$ and $B$ in this coordinate system can be written by different potential energies at $A$ and $B$ points as:

$$W_{AB} = U_A - U_B \tag{3.20}$$

because $\mathbf{F_i}$ , the conservative force of the $i^{th}$ particle, can be expressed as:

$$W_{AB} = \int_A^B \mathbf{F_i} \cdot d\mathbf{l} \qquad \mathbf{F_i} = -\nabla_i U, \tag{3.21}$$

where the $F_i$ and $U$ are the functions of $\mathbf{r_i}$, the distances of $i^{th}$ particles. (In this case, the external force, electric force is conservative force.)

Because of classical behavior of this system and each particle separately, the acceleration of the $i^{th}$ particle according to Newton's second law can be written as:

$$\mathbf{a_i} = \ddot{\mathbf{r}}_\mathbf{i} = \mathbf{F_i}/m_i. \tag{3.22}$$

With the velocities of each particles, $\{\dot{\mathbf{r}}_\mathbf{1}, \dot{\mathbf{r}}_\mathbf{2}, \cdots, \dot{\mathbf{r}}_\mathbf{n}\}$, the kinetic energy is:

$$K(\dot{r}_1, \dot{r}_2, \cdots, \dot{r}_n) = \frac{1}{2} \sum_{i=1}^N m_i \dot{\mathbf{r}}_\mathbf{i}^2 \tag{3.23}$$

where distinguishes the dynamic method from the former static one.

It means the total energy is:

$$E = \frac{1}{2} \sum_{i=1}^N m_i \dot{\mathbf{r}}_\mathbf{i}^2 + U(\mathbf{r}_1, \mathbf{r}_2, \cdots, \mathbf{r}_n). \tag{3.24}$$

Assuming the internal force is pairwise additive and there is a external force (electric force in this case) the $\mathbf{F_i}$ is relevant to the positions of every particles and the velocity of

the $i^{th}$ particle as:

$$\mathbf{F_i}(\mathbf{r_1}, \mathbf{r_2}, \cdots, \mathbf{r_n}, \dot{\mathbf{r}_i}) = \sum_{j \neq i} \mathbf{F_{ij}^{int}}(\mathbf{r_i} - \mathbf{r_i}) + \mathbf{F^{ext}}(\mathbf{r}_i, \dot{\mathbf{r}_i}) = m_i \ddot{\mathbf{r}_i} \qquad (3.25)$$

With the given initial values of position $\mathbf{r_i^0}$ and velocity $\dot{\mathbf{r}_i^0}$ for $i^{th}$ particle, the problem can be described as:

$$\frac{d^2}{dt^2}\mathbf{r_i} = \frac{d}{dt}\dot{\mathbf{r}_i} = \ddot{\mathbf{r}_i} = \mathbf{a_i}$$
$$\dot{\mathbf{r}_i} = \dot{\mathbf{r}_i^0} + \mathbf{a_i}t \qquad (3.26)$$
$$\mathbf{r_i} = \mathbf{r_i^0} + \dot{\mathbf{r}_i^0}t + \frac{1}{2}\mathbf{a_i}t^2$$

The essential concept of molecular dynamics is above. Each atom of the system is viewed as the object with classical behavior even the interaction between any two atom (internal force) is considered as intermolecular force. The steps to get the trajectory of any atom in the system are as follows:
(1) The new force and acceleration of every atom in the system can be calculated by (3.21) and (3.22);
(2) Ones new position and velocity can be calculated by (3.26) with given time step;
(3) Repeat (1) and (2) to obtain the data of positions, velocities, accelerations of each atoms.

In addition, the calculation with molecular dynamics has three important aspects to be paid attention to as follows [Tuckerman, 2010]:
(1) the model describing the interparticle interactions (what this work concerns in chapter 3.1);
(2) the calculation of energies and forces from the model (what chapter 3.2 introduces);
(3) the algorithm used to integrate the equations of motion.
All of these three aspects mentioned above have strong influences on the quality of the calculation.

**Numerical Integration Scheme**

The most common integration scheme to calculate the position $\mathbf{r_i}$ of the $i^{th}$ particle at any time $t$ with molecular dynamic method is Verlet algorithm as:

$$\mathbf{r_i}(t + \delta t) = 2\mathbf{r_i}(t) - 2\mathbf{r_i}(t - \delta t) + \frac{\delta t^2}{m_i}\mathbf{F_i}(t), \qquad (3.27)$$

where $\delta t$ is the time step. And the velocity $\dot{\mathbf{r}_i}$ at $t$ is:

$$\dot{\mathbf{r}_i}(t) = \frac{\mathbf{r_i}(t + \delta t) - \mathbf{r_i}(t - \delta t)}{2\delta t} \qquad (3.28)$$

It is obvious that the calculation with $\frac{1}{\delta t}$ will introduce large error for small $\delta t$.

The velocity Verlet algorithm can solve this problem with follows:

$$
\begin{aligned}
\mathbf{r_i}(t) &= \mathbf{r_i}(t + \delta t) - \delta t \dot{\mathbf{r}}_\mathbf{i}(t + \delta t) + \frac{\delta t^2}{2m_i}\mathbf{F_i}(t) \\
\dot{\mathbf{r}}_\mathbf{i}(t + \delta t) &= \dot{\mathbf{r}}_\mathbf{i}(t) + \frac{\delta t}{2m_i}[\mathbf{F_i}(t) + \mathbf{F_i}(t + \delta t)]
\end{aligned}
\tag{3.29}
$$

The leap frog method is another way to solve this problem as:

$$
\begin{aligned}
\dot{\mathbf{r}}_\mathbf{i}(t + \frac{1}{2}\delta t) &= \dot{\mathbf{r}}_\mathbf{i}(t - \frac{1}{2}\delta t) + \frac{\mathbf{F_i}(t)}{m_i}\delta t \\
\mathbf{r_i}(t + \delta t) &= \mathbf{r_i}(t) + \dot{\mathbf{r}}_\mathbf{i}(t + \frac{1}{2}\delta t)\delta t
\end{aligned}
\tag{3.30}
$$

**Thermal Equilibrium and Ensembles**

Two main thermodynamic theorems aid the understanding of thermal equilibrium and the ensembles which will be introduced later.

The first law of thermodynamics states the conservation of energy as in any thermodynamic transformation, if a system absorbs an amount of heat $\delta Q$ and has an amount of work $\delta W$ performed on it, then its internal energy will change by an amount $\delta E$ given by [Tuckerman, 2010]:

$$
\delta E = \delta W + \delta Q
\tag{3.31}
$$

The second law of thermodynamics states the behavior of the entropy in any thermodynamic transformation as in any thermodynamic transformation, the total entropy of the universe must either increase or remain the same [Tuckerman, 2010].
And the entropy $S$ is defined as:

$$
dS = \frac{dQ_{rev}}{T},
\tag{3.32}
$$

where $Q_{rev}$ is the amount of the heat in the reversible process and $T$ is temperature. When $dS = 0$, the isolated system does neither absorb nor release heat.

Assuming there are two systems can only change heat as figure 3.7.

The entropies of two systems are:

$$
\begin{aligned}
S_1(N_1, V_1, E_1) &= Kln\Omega_1(N_1, V_1, E_1) \\
S_2(N_2, V_2, E_2) &= Kln\Omega_2(N_2, V_2, E_2)
\end{aligned}
\tag{3.33}
$$

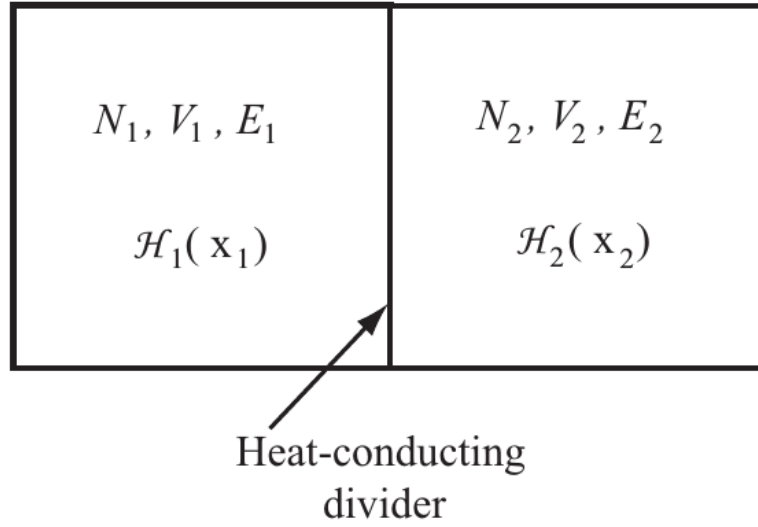where $\Omega$ is the partition functions of Hamilton's equations.

**Figure 3.7:** Two systems can only change heat. system 1 (left) has $N_1$ particles in a volume $V_1$; system 2 (right) has $N_2$ particles in a volume $V_2$. [Tuckerman, 2010]

Thermal equilibrium for these two systems means:

$$T_1 = T_2 \tag{3.34}$$

According to two thermodynamic laws, the total energy change can be described as:

$$dE = TdS - PdV + \mu dN, \tag{3.35}$$

where $\mu$ is a function of N.

That means the entropy $S$ is:

$$dS = \frac{1}{T}dE + \frac{P}{T}dV - \frac{\mu}{T}dN \tag{3.36}$$

Since the entropy of a certain system depends on 3 variables N, V, E, ($S = S(N, V, E)$), the common ensemble always changes entropy by changing these three control variables to obtain the thermodynamic results in the thermal equilibrium.

There are four common ensembles for molecular dynamic method in thermal equilibrium, such as:

(1) micro-canonical ensemble (NVE). The system with this ensemble has certain number of particles $N$, volume $V$ and total energy $E$ with small disturbances of temperature and pressure around at given data. It is the common ensemble for molecular dynamic method. The system in the equilibrium is isolated.

(2) canonical ensemble (NVT). The system with this ensemble has certain number of

particles $N$, volume $V$ and temperature $T$. It is the common ensemble for Monte Carlo method.

(3) classical isotropic isothermal-isobaric ensemble (NPT). The system with this ensemble has certain number of particles $N$, pressure $P$ and temperature $T$. It is always utilized for phase transition.

(4) isenthalpic ensenmble (NPH). The system with this ensemble has certain number of particles $N$, pressure $P$ and enthalpy $H$. It is rarely utilized nowadays.

Limitations of space prevent us from the introductions of another two important aspects which should be considered: the number of the atoms in a certain molecular system with molecular dynamic method and the selections of initial values (such as the initial positions of atoms and integration time step). The former one can estimate the time consuming and the latter one influences the run time and the occupied storage space. The thermal equilibrium also depends on the suitable initial value.

### 3.2.3 Monte Carlo Method

It is the first method applied in the molecular simulation field with stochastic methods to generate the results. The thermal and electric properties at nonzero temperatures in large numbers of atoms can be calculated by Monte Carlo method. It cannot be used to calculate the motions of the particles because of its properties.

# 4

# SIMULATIONS AND NUMERICAL RESULTS

This chapter presents that if the thin film with shrink-wrapped boundary condition in z-direction emerges ferrroelectric property by plotting the hysteresis loops and observing the spontaneous polarizations. All of the results are generated using the LAMMPS software.

The simulations are based on the molecular static method with the periodic boundary condition in x- and y-direction as well as the shrink-wrapped boundary condition in z-direction. The parameters for core-shell model of $BaTiO_3$ are in table 3.1 and the lattice constants of rhombohedral state are in table 2.2.

## 4.1 Simulation

Because of the existing codes, especially the special output codes, in the library of LAMMPS, the simulation by LAMMPS has a secondary development for calculation of polarization per atom.

Due to the requirements of loops in LAMMPS, another pre- and post-processors participate the simulations.
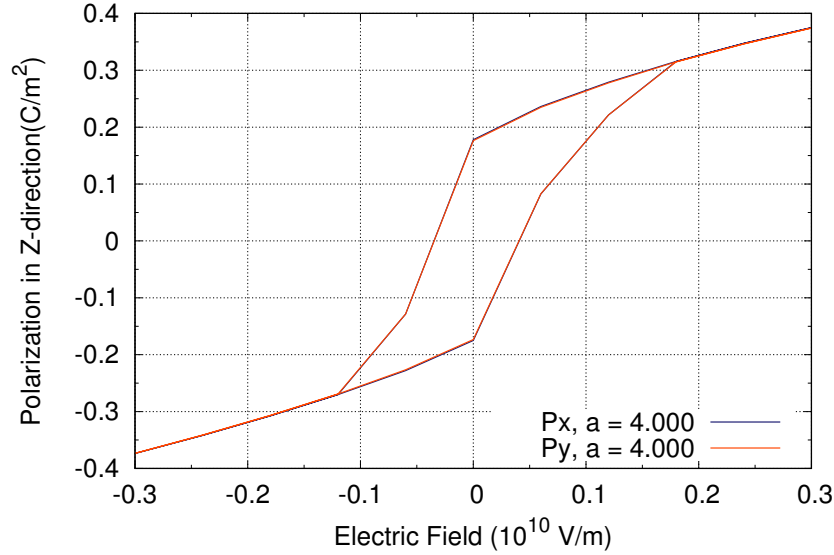
### 4.1.1 Preprocessor



**Figure 4.1:** Hysteresis loops in x- and y-direction with $a = 4.000$ $\alpha = 89°54$ in $6 \times 6 \times 8$ unit cells system. (step length $= 0.06 * 10^{10}$ V/m and range of strength of electric field is $[-0.3, 0.3] * 10^{10}$ V/m.)

For the loop code, LAMMPS defines that the variables cannot be changed after giving the pair and bond coefficients. With using the loop in LAMMPS directly, the results are generated as the isolated values, which means the latter polarization for the corresponding strength of electric field is independent on the former corresponding strength of the electric field, in the given range instead of the values along a path with the corresponding changing strengths of the electric field.

In order to solve this problem, a preprocessor is introduced to generate a new file for the loop part to do the simulation by molecular statics with the changing strengths of the electric fields. It generates a new file (LAMMPS running file) and at the end of the operation of the old file with parameters will "jump" into the new one according to a command named "jump" in LAMMPS. The polarizations in x- and y-direction with the preprocessor are as figure 4.1. In order to read the data file after the first step by postprocessor, there is a line of codes asked the count of the time step in the loop to reset (back to 0) once the calculations begin for the new strengths of electric fields, which is named as "reset_timestep 0".

### 4.1.2 Secondary Development for LAMMPS

The calculator for polarization per atom is a secondary development, because there is no such function in the library of LAMMPS. As for the reason why not develop the

polarization of the entire system directly, there is no output file which can support to generate the result for the system. The volume used in the polarization per atom file is the instantaneous volume of the system from the output data for the "thermo_style" iterations.

### 4.1.3 Postprocessor

The data generated by the operation in LAMMPS are in a very large file. The postprocessor is utilized for calculating the polarization of the system by this data file.

The generated file by preprocessor and LAMMPS will print out one sentence as "TIMESTEP 0" at the beginning of every new simulation corresponding to the new strength of electric field. LAMMPS does not support to open and save data in the new files with the changing strengths of electric fields, or the polarizations will be the isolated results as same as what is described in the first paragraph of section 4.1.1. That is why the large data file is generated for this simulation by LAMMPS.

The postprocessor divides the large data file into several (the number of strengths of electric field) smaller ones according to the sentence as "TIMESTEP 0" at the first step. Then the postprocessor ignores the first several lines (more than 100,000 for a $6 * 6 * 8$ system, which depends on the difference of the number of lines in the smaller data files and the number of atoms,) and just reads the last several lines (the number of atoms, which is equal to 10 times the number of unit cells in the simulation for this work) and calculates the polarizations of the system.

## 4.2 Numerical Results

The molecule of $BaTiO_3$ by Ovito is as figure 4.2. The three yellow spheres symbolize the O-ion, the white one symbolizes Ti-ion and the blue one symbolizes Ba-ion.

The $6 \times 6 \times 8$ unit cells system in three dimension, which is consisted of $6 \times 6 \times 8$ single unit cells like figure 4.2, is as figure 4.3.(generated by Moltemplate and shown by Ovito):

All of the strengths of the electric fields in Chapter 4 is the total strengths of the electric fields, the ones in three directions are same. The magnitude of the strength of the electric field is $10^{10}$ V/m because of the unit in LAMMPS.

With periodic boundary condition, it is easy to get the hysteresis in x- and y-direction even for the $6 \times 6 \times 8$ unit cells system as figure 4.1. Therefore the hysteresis loop will not be depict anymore in the following figures.
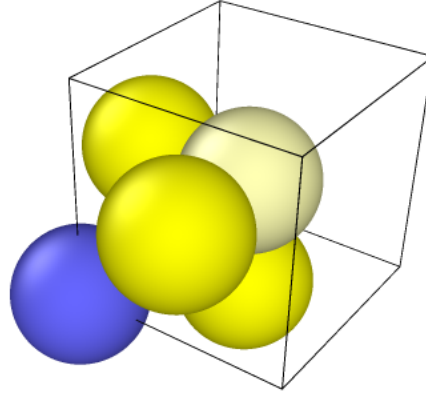
**Figure 4.2:** The single unit cell of $BaTiO_3$. (Ovito)

## 4.2.1 Result for the Purpose of this Work

There is a hysteresis loop in z-direction with the shrink-wrapped boundary condition in $10 \times 10 \times 12$ unit cells system when $a = 4.000 \; \alpha = 89°54'$, event though the coercive fields, the two values of the strengths of electric fields corresponding the polarizations in z-direction are 0, are really small. And the remanent polarizations are also small. In order to obtain the better result, the larger range can be used for the searching of the maximum values of the coercive fields. Figure 4.5-4.7 as followings show there is a weak ferroelectricity in $6 \times 6 \times 8$ unit cells system and figure 4.8 shows $10 \times 10 \times 16$ unit cells system does not reach the suitable range of external electric field for the hysteresis with the one used for $10 \times 10 \times 12$ unit cells system.

## 4.2.2 Different Influences on Polarizations with Different Parameters

Several different polarizations in z-direction with shrink-wrapped boundary condition corresponding to different ranges and step lengths, different ranges, different lattice constants, different thicknesses and different systems with different ranges are calculated in this part, which will be helpful to improve the hysteresis in z-direction in $10 \times 10 \times 12$ unit cells system in the future.
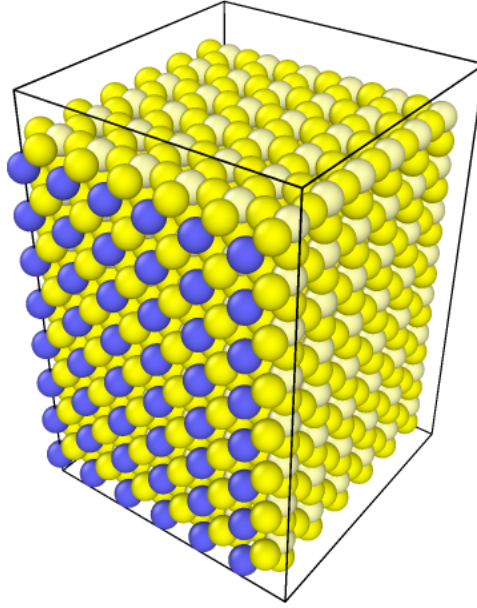
**Figure 4.3:** $6 \times 6 \times 8$ unit cells system. (Ovito)

## Different Ranges and Step Lengths

Figure 4.5 shows the hysteresis loops in z-direction with lattice constants $a = 4.010 \alpha = 89°81'$ in $6 \times 6 \times 8$ unit cells system with different step lengths of strength of electric field as $0.036 * 10^{10} V/m$, $0.02 * 10^{10} V/m$ in different ranges as $[-0.18, 0.18] * 10^{10} V/m$ and $[-0.2, 0.2] * 10^{10} V/m$. With the decreasing of the step length and increasing of range, the configuration of the hysteresis is "wider" and two different coercive fields appear even though there is only one "remanent polarization". The chosen of the range of strength of electric field are important to the polarizations in z-direction with free-energy boundary condition.

## Different Ranges

Figure 4.6 shows the hysteresis loops in z-direction with lattice constants $a = 4.010 \alpha = 89°81'$ in $6 \times 6 \times 8$ unit cells system with different ranges of the strengths of electric fields as $[-0.2, 0.2] * 10^{10} V/m$, $[-0.1, 0.1] * 10^{10} V/m$. It is obvious that the smaller range of the strength of electric field will get the smaller hysteresis loop. With the increasing of range, the changes of the hysteresis loops are same as the one in the section of different ranges and step lengths. The chosen of the range of strength of electric field is more important to the polarizations in z-direction with free-energy boundary condition when the maximum coercive field is not reached.
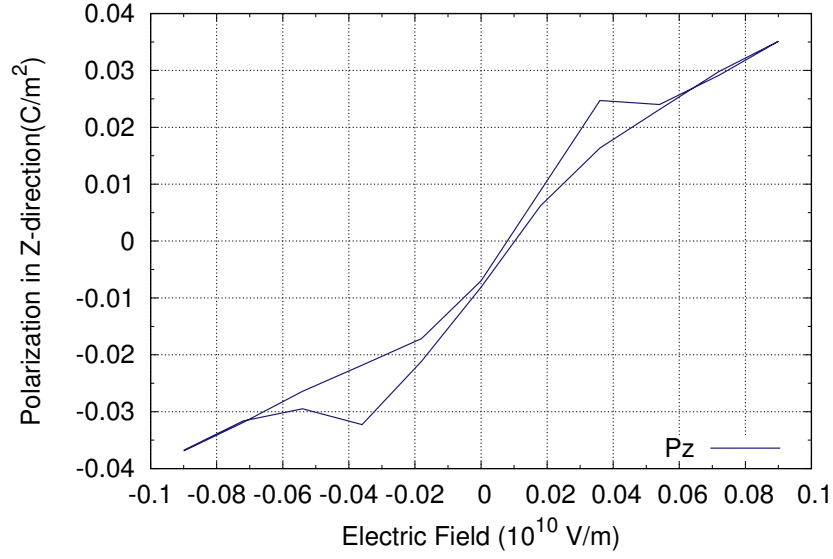
**Figure 4.4:** Hysteresis loop in z-direction with $a = 4.000$ $\alpha = 89°54'$ in $10 \times 10 \times 12$ unit cells system. (step length = $0.02 * 10^{10}$ V/m and range of strength of electric field is $[-0.9, 0.9] * 10^{10}$ V/m.)

### Different Lattice Constants

The hysteresis loops with different lattice constants $a = 4.010$ $\alpha = 89°81'$ [Vielma and Schneider, 2013], $a = 3.998$ $\alpha = 89°52.5'$, as shown in table 2.1, in $6 \times 6 \times 8$ unit cell system with same step length of strength of electric field $0.02 * 10^{10} V/m$ are as figure 4.7. The configuration of the hysteresis loops are nearly same for different lattice constants, which means the lattice constants have less influence on the hysteresis in z-direction of this work.

The $a = 4.000$ $\alpha = 89°54'$ are chosen as the lattice constants for figure 4.1, 4.4, 4.8-10.

### The Different Thickness in $10 \times 10 \times n_z$ Unit Cells System

With the same lattice constants $a = 4.000$ $\alpha = 89°54'$ in $10 \times 10 \times n_z$ unit cells system, the hysteresis loops are shown in figure 4.8. It is obvious that there is hysteresis loops when $n_z$ is 12 unit cells but a strange loop for 16 unit cells. The configurations of these two hysteresis loops are nearly same except for the coercive field part and the remanent polarizations. The thicker slab need a new suitable range of the strength of the electric field to obtain the hysteresis loop.

**The Different Number of Unit Cells System**

With the same lattice constants $a = 4.000$ $\alpha = 89°54'$ in $6 \times 6 \times 8$ unit cells system and $10 \times 10 \times 12$ unit cells system, the hysteresis loops are shown in figure 4.9. It is obvious that $6 \times 6 \times 8$ unit cells system can not get a fine hysteresis loop in this range. The increasing number of unit cells system will improve the hysteresis loop in z-direction with the free-energy boundary condition when the suitable range is found.

## 4.3 The Polarizations with Changing Thicknesses

The polarizations with changing thicknesses of $10 \times 10 \times 12$ system when the strength of electric field is $0.02 * 10^{10}$ $V/m$ is as figure 4.10. It is obvious that the polarzations are increasing with the incremental number of unit cells in z-direction. It means the field the system simulates is expanding with the increasing $n_z$ because the calculations of polarizations used in this work is related to the displacements of the cores of the ions (molecular statics). Higher polarization in z-direction means that the cores of the ions have moved more along z-direction.
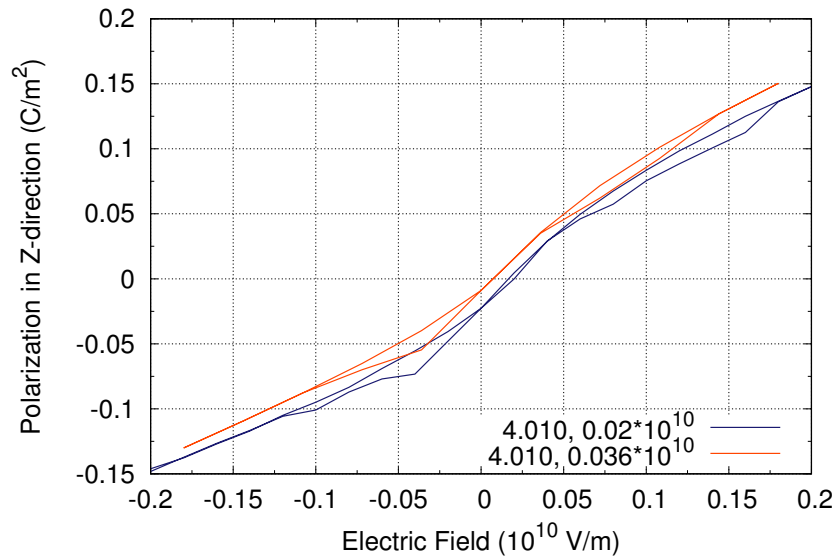


**Figure 4.5:** Hysteresis loop in z-direction with $a = 4.010$ $\alpha = 89°81'$ in $6 \times 6 \times 8$ unit cells system. (step length $= 0.02 * 10^{10}$ V/m and $0.036 * 10^{10}$ V/m in the range of strength of electric field $[-0.2, 0.2] * 10^{10}$ V/m and $[-0.18, 0.18] * 10^{10}$ V/m.)
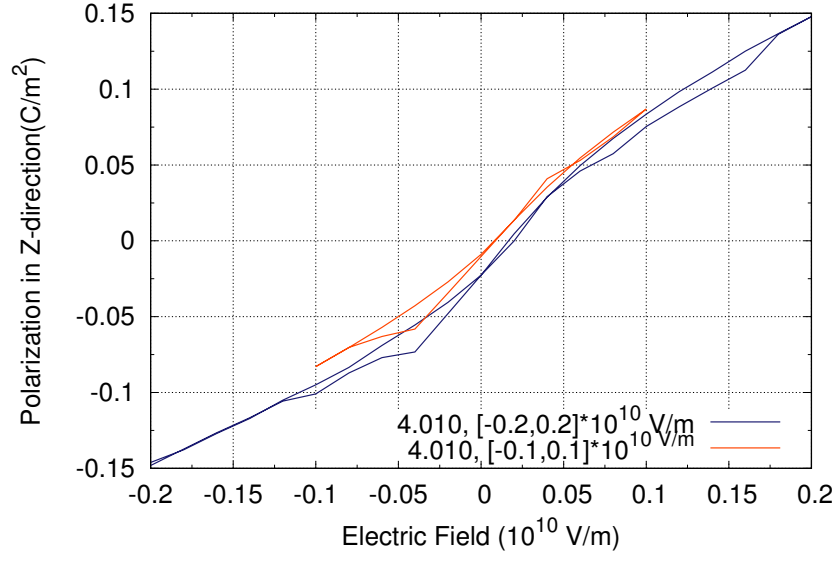
**Figure 4.6:** Hysteresis loop in z-direction with $a = 4.010$ $\alpha = 89°81'$ in $6 \times 6 \times 8$ unit cells system, step length is $0.02 * 10^{10}$ V/m in the range of $[-0.2, 0.2] * 10^{10}$ V/m and $[-0.1, 0.1] * 10^{10}$ V/m.
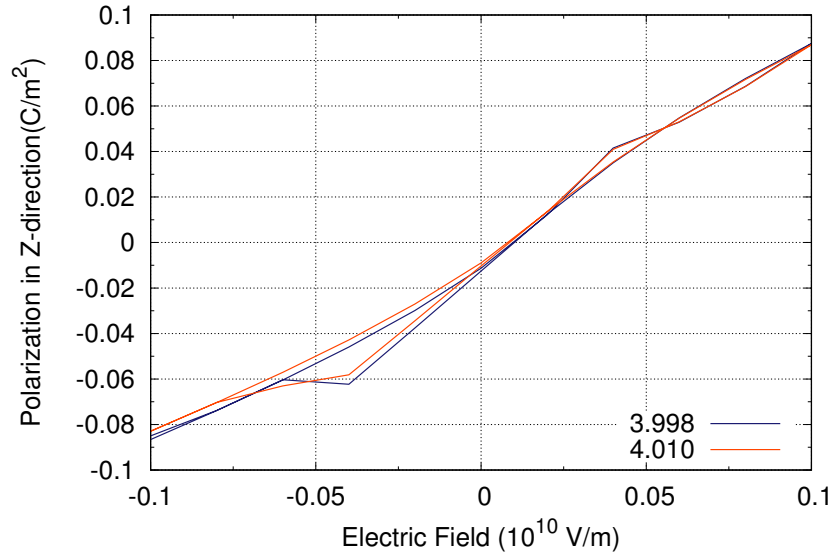


**Figure 4.7:** Hysteresis loop in z-direction with $a = 3.998$ $\alpha = 89°52.5'$ and $a = 4.010$ $\alpha = 89°81'$ in $6 \times 6 \times 8$ unit cells system.
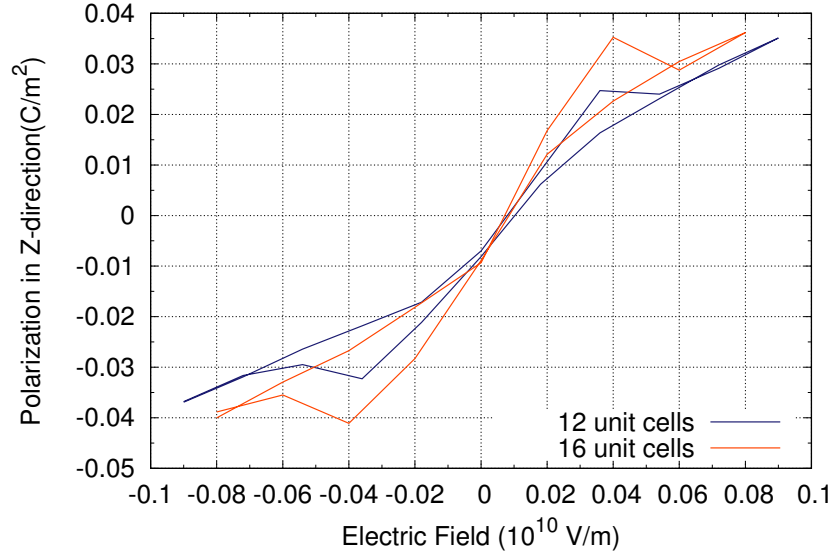
**Figure 4.8:** Hysteresis loop in z-direction with $a = 4.000\ \alpha = 89°54'$ in $10 \times 10 \times nz$ unit cells system, when nz = 12 and 16 unit cells.
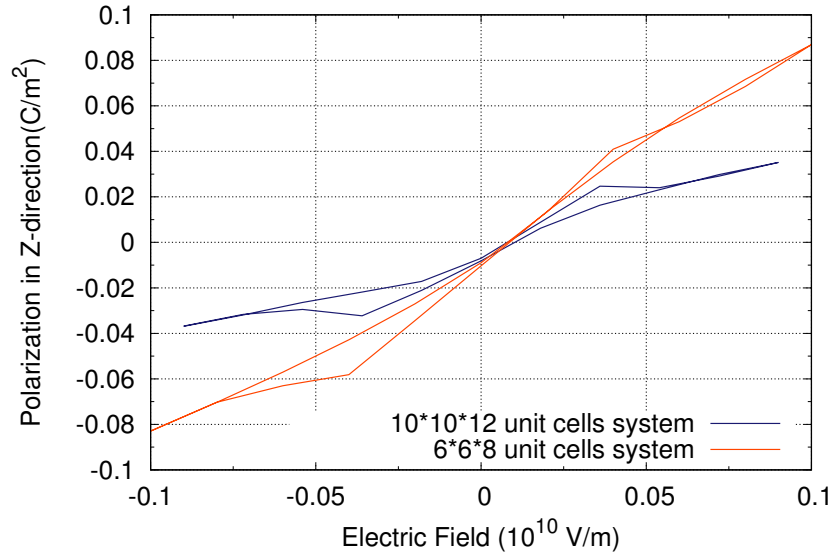


**Figure 4.9:** Hysteresis loop in z-direction with $a = 4.000\ \alpha = 89°54'$ in $10 \times 10 \times 12$ (range of electric field: $[-0.09, 0.09] * 10^{10}$ V/m) and $6 \times 6 \times 8$ unit cells system (range of electric field: $[-0.1, 0.1] * 10^{10}$ V/m) .
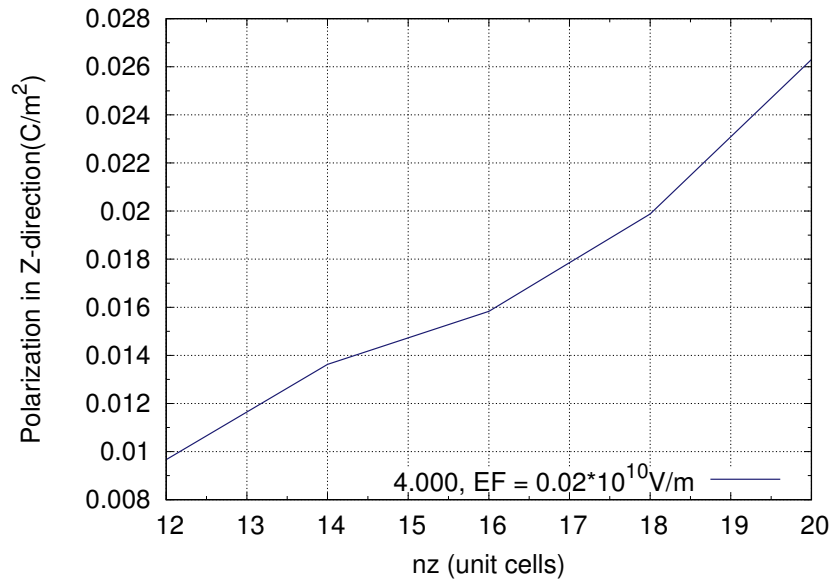
**Figure 4.10:** Changing thicknesses for $10 \times 10 \times 12$ unit cells system when strength of electric field is $0.02 * 10^{10}$ V/m.

# 5

# CONCLUSION AND FUTURE WORK

## 5.1 Conclusion

Through molecular statics simulations it is shown that ferroelectricity emerges in $BaTiO_3$ ultrathin films even at a thickness of 48 Å (12 unit cells). Along the lateral directions in ultrathin films, the ferroelectricity is retained and comparable to that of bulk materials. Along the thickness of ferroelectric, the presence of more unit cells in a system will generate more prominent ferroelectric hysteresis loops by molecular static method. The reason of "narrow" coercive field of the polarizations in z-direction might be the velocities in z-direction with free-energy boundary condition will be larger for less unit cells around at electric field = 0 or , the most important reason, the range of the electric field is not large enough. The more accurate result might appear for the larger range of electric field with smaller step length by molecular statics.

Different lattice constants, different bond and pair coefficients for the simulations with other same parameters will generate different polarizations. The range of the strengths of the electric field plays a really important role in the calculations of polarizations.

Different step length of strength of electric field is more important to the range of the polarizations the simulation can get and smaller range of the strength of electric field which can get the hysteresis loop will get the smaller hysteresis loop. The lattice constants have more influence on the results corresponding to the strength of electric fields with shrink-wrapped boundary condition.

## 5.2 Future Work

On the one hand, the ferroelectric slab could to be delved into the properties with the different simulation models, such as bond-valence model. The properties part can be generated by molecular dynamic method, which also considers the kinetic energy of the atoms in the system. The thicker ferroelectric thin film should also be investigated.

On the other hand, current status and trends in the researches of ferroelectrics is to reduce the dimensionality of this kind of materials. This work investigates the ultrathin films in 2 dimensional case with periodic boundary conditions, which means both the nanolines in 1 dimensional case with periodic boundary condition and the nanodots with the same boundary condition can be the highlights for the ferroelectric materials in the future.

# Bibliography

CH Ahn, KM Rabe, and J-M Triscone. Ferroelectricity at the nanoscale: local polarization in oxide thin films and heterostructures. *Science*, 303(5657):488–491, 2004.

JD Axe. Apparent ionic charges and vibrational eigenmodes of bati o 3 and other perovskites. *Physical Review*, 157(2):429, 1967.

I P° Batra and BD Silverman. Thermodynamic stability of thin ferroelectric films. *Solid State Communications*, 11(1):291–294, 1972.

JD Bernal and RH Fowler. A theory of water and ionic solution, with particular reference to hydrogen and hydroxyl ions. *The Journal of Chemical Physics*, 1(8):515–548, 1933.

Relva C Buchanan. *Ceramic materials for electronics*, volume 68. CRC press, 2004.

Alexander V Bune, Vladimir M Fridkin, Stephen Ducharme, Lev M Blinov, Serguei P Palto, Alexander V Sorokin, SG Yudin, and A Zlatkin. Two-dimensional ferroelectric films. *Nature*, 391(6670):874–877, 1998.

Kevin M Chen, Andrew W Sparks, Hsin-Chiao Luan, Desmond R Lim, Kazumi Wada, and Lionel C Kimerling. Sio 2/tio 2 omnidirectional reflector and microcavity resonator via the sol-gel method. *Applied Physics Letters*, 75(24):3805–3807, 1999.

Long-Qing Chen. Phase-field method of phase transitions/domain structures in ferroelectric thin films: A review. *Journal of the American Ceramic Society*, 91(6):1835–1844, 2008.

M Dawber, KM Rabe, and JF Scott. Physics of thin-film ferroelectric oxides. *Reviews of modern physics*, 77(4):1083, 2005.

Martin T Dove. An introduction to atomistic simulation methods. *Seminarios de la SEM*, 4:7–37, 2008.

Florian Endres and Paul Steinmann. Molecular statics simulations of ferroelectric barium titanate in the rhombohedral phase. *GAMM-Mitteilungen*, 38(1):132–146, 2015.

AE Feuersanger, AK Hagenlocher, and AL Solomon. Preparation and properties of thin barium titanate films. *Journal of The Electrochemical Society*, 111(12):1387–1391, 1964.

Alessio Filippetti and Nicola A Spaldin. Strong-correlation effects in born effective charges. *Physical Review B*, 68(4):045111, 2003.

Dillon D Fong, G Brian Stephenson, Stephen K Streiffer, Jeffrey A Eastman, Orlando

Auciello, Paul H Fuoss, and Carol Thompson. Ferroelectricity in ultrathin perovskite films. *Science*, 304(5677):1650–1653, 2004.

Jan Fousek. Joseph valasek and the discovery of ferroelectricity. In *Applications of Ferroelectrics, 1994. ISAF'94., Proceedings of the Ninth IEEE International Symposium on*, pages 1–5. IEEE, 1991.

Ph Ghosez and KM Rabe. Microscopic model of ferroelectricity in stress-free pbtio 3 ultrathin films. *Applied Physics Letters*, 76(19):2767–2769, 2000.

Ph Ghosez, Xavier Gonze, Ph Lambin, and J-P Michenaud. Born effective charges of barium titanate: Band-by-band decomposition and sensitivity to structural features. *Physical Review B*, 51(10):6765, 1995.

Ph Ghosez, J-P Michenaud, and Xavier Gonze. Dynamical atomic charges: The case of ab o 3 compounds. *Physical Review B*, 58(10):6224, 1998.

Gene H Haertling. Ferroelectric ceramics: history and technology. *Journal of the American Ceramic Society*, 82(4):797–818, 1999.

Javier Junquera and Philippe Ghosez. Critical thickness for ferroelectricity in perovskite ultrathin films. *Nature*, 422(6931):506–509, 2003.

John N Lalena and David A Cleary. *Principles of inorganic materials design*. John Wiley & Sons, 2010.

Sidney B Lang. *Sourcebook of pyroelectricity*, volume 2. CRC Press, 1974.

Céline Lichtensteiger, Matthew Dawber, and Jean-Marc Triscone. Ferroelectric size effects. In *Physics of ferroelectrics*, pages 305–338. Springer, 2007.

Malcolm E Lines and Alastair M Glass. *Principles and applications of ferroelectrics and related materials*. Oxford university press, 1977.

Costas D Maranas and Christodoulos A Floudas. Global minimum potential energy conformations of small molecules. *Journal of Global Optimization*, 4(2):135–170, 1994.

J-C Niepce and L Pizzagalli. Structure and phase transitions in nanocrystals. In *Nanomaterials and Nanochemistry*, pages 35–54. Springer, 2008.

Takeshi Nishimatsu, Umesh V Waghmare, Yoshiyuki Kawazoe, and David Vanderbilt. Fast molecular-dynamics simulation for ferroelectric thin-film capacitors using a first-principles effective hamiltonian. *Physical Review B*, 78(10):104104, 2008.

Masanori Okuyama and Yoshihiro Ishibashi. *Ferroelectric thin films: basic properties and device physics for memory applications*, volume 98. Springer Science & Business Media, 2005.

Simon R Phillpot, Susan B Sinnott, and Aravind Asthagiri. Atomic-level simulation of ferroelectricity in oxides: Current status and opportunities. *Annu. Rev. Mater. Res.*, 37:239–270, 2007.

Karin M Rabe, Charles H Ahn, and Jean-Marc Triscone. *Physics of ferroelectrics: a modern perspective*, volume 105. Springer Science & Business Media, 2007.

WG Ralph. Wyckoff: Crystal structure. In *Inorganic Compounds RXn, RnMX2, RnMX3*, volume 2. John Wiley & Sons, 1964.

R Resta. Polarization as a berry phase. *Europhysics News*, 28(1):18–20, 1997.

Na Sai, Alexie M Kolpak, and Andrew M Rappe. Ferroelectricity in ultrathin perovskite films. *Physical Review B*, 72(2):020101, 2005.

Yongliang Sang, Bin Liu, and Daining Fang. The size and strain effects on the electric-field-induced domain evolution and hysteresis loop in ferroelectric batio 3 nanofilms. *Computational Materials Science*, 44(2):404–410, 2008.

James F Scott. *Ferroelectric memories*, volume 3. Springer Science & Business Media, 2013.

James F Scott and Carlos A Paz De Araujo. Ferroelectric memories. *Science*, 246(4936): 1400–1405, 1989.

M Sepliarsky, A Asthagiri, SR Phillpot, MG Stachiotti, and RL Migoni. Atomic-level simulation of ferroelectricity in oxide materials. *Current Opinion in Solid State and Materials Science*, 9(3):107–113, 2005.

N Setter, D Damjanovic, L Eng, G Fox, Spartak Gevorgian, S Hong, A Kingon, H Kohlstedt, NY Park, GB Stephenson, et al. Ferroelectric thin films: Review of materials, properties, and applications. *Journal of Applied Physics*, 100(5):051606, 2006.

Young-Han Shin, Valentino R Cooper, Ilya Grinberg, and Andrew M Rappe. Development of a bond-valence molecular-dynamics model for complex oxides. *Physical Review B*, 71(5):054104, 2005.

JR Slack and JC Burfoot. Flash evaporation of ferroelectric thin films. *Thin Solid Films*, 6(4):233–237, 1970.

Alexander Stukowski. Visualization and analysis of atomistic simulation data with ovito–the open visualization tool. *Modelling and Simulation in Materials Science and Engineering*, 18(1):015012, 2009.

James William Thomas. *Numerical partial differential equations: finite difference methods*, volume 22. Springer Science & Business Media, 2013.

DR Tilley and Boštjan Žekš. Landau theory of phase transitions in thick films. *Solid State Communications*, 49(8):823–828, 1984.

S Tinte and MG Stachiotti. Surface effects and ferroelectric phase transitions in batio 3 ultrathin films. *Physical Review B*, 64(23):235403, 2001.

Mark Tuckerman. *Statistical mechanics: theory and molecular simulation*. Oxford University Press, 2010.

Thomas Tybell, CH Ahn, and J-M Triscone. Ferroelectricity in thin perovskite films. *Applied physics letters*, 75(6):856–858, 1999.

Jason M Vielma and Guenter Schneider. Shell model of batio3 derived from ab-initio total energy calculations. *Journal of Applied Physics*, 114(17):174108, 2013.

A Von Hippel, RG Breckenridge, FG Chesley, and Laszlo Tisza. High dielectric constant ceramics. *Industrial & Engineering Chemistry*, 38(11):1097–1109, 1946.

Vinod Wadhawan. *Introduction to ferroic materials*. CRC press, 2000.

JJ Wang, FY Meng, XQ Ma, MX Xu, and LQ Chen. Lattice, elastic, polarization, and electrostrictive properties of batio 3 from first-principles. *Journal of Applied Physics*, 108(3):034107, 2010.

R Waser and DM Smyth. Defect chemistry, conduction, and breakdown mechanism of perovskite-structure titanates. *Ferroelectric thin films: Synthesis and basic properties, ferroelectricity and related phenomena*, 10:47–92, 1996.

N Scott Weingarten and James P Larentzos. Implementation of shifted periodic boundary conditions in the large-scale atomic/molecular massively parallel simulator (lammps) software. Technical report, ARMY RESEARCH LAB ABERDEEN PROVING GROUND MD WEAPONS AND MATERIALS RESEARCH DIRECTORATE, 2015.

W Zhong, RD King-Smith, and David Vanderbilt. Giant lo-to splittings in perovskite ferroelectrics. *Physical review letters*, 72(22):3618, 1994.